Structural and Electrical Characterisation of Silicon and other Semiconducting Nanoparticle Networks for use in Sensor and Photovoltaic Applications

R.K. Setshedi

(STSRHY001)

Supervisor: Prof. D.T. Britton

Co-Supervisor: Prof. M. Härting

Thesis presented for the degree of

DOCTOR OF PHILOSOPHY

in the Department of Physics

Faculty of Science

UNIVERSITY OF CAPE TOWN

Version date : May 13, 2016

Acknowledgments

First and foremost I would like to thank my Lord and Saviour Jesus Christ who ordained this journey for me. May all the glory and honour be to Him.

This work would not have been possible without my two lovely supervisors:- Prof. David Britton and Prof. Margit Härting who tirelessly guided me through this process. Special thanks goes to my brother in the Lord Dr Emmanuel Ohieku Jonah, who burned the midnight oil with me while making sense of the results section of this research. To my dearest Marie-Anne, thank you for doing a sterling job in correcting the language aspect of this report. Thank you Vidius Archer for your encouragement and support.

Many thanks to Prof. G. Beaucage, Dr. J. Ilavsky, Dr. G. Smith, Dr. D.K. Rai and Dr. E.O. Jonah for conducting the USAXS experiment on my samples at the Advance Photon Source - Argonne National Laboratory. ChemMatCARS Sector 15 is principally supported by the Divisions of Chemistry (CHE) and Materials Research (DMR), National Science Foundation, under grant number NSF/CHE-1346572. Use of the Advanced Photon Source, an Office of Science User Facility operated for the U.S. Department of Energy (DOE) Office of Science by Argonne National Laboratory, was supported by the U.S. DOE under Contract No. DE-AC02-06CH11357.

A big thanks also goes to my colleagues : - Serges, Claire, Florence, David, Steve, Stanley and Batsirai for always being willing to share their thoughts and expertise with me.

Lastly, thanks to the “Almighty”, for giving me a lovely wife, “Tsotso” to whom I owe the success of this project.

Abstract

Silicon nanoparticles are increasingly being used as the active layer in electronic materials such as field effect transistors and negative temperature coefficient thermistors [1–3]. These devices can be printed at low-temperatures on flexible substrates such as paper [3, 4]. The efficiency of these electronic devices relies on the physical, hence electrical characteristics of their constituent nanoparticle networks and clusters.

However, structural characterisation of these random networks of particles presents a formidable challenge due to their size, mobility and state. In this research project, an inhouse laboratory based Small Angle Light Scattering experiment has been successfully used to extend the low q-range of the Ultra Small Angle X-ray Scattering technique by close to an order of magnitude, thereby increasing the sensitivity of this technique to quantitatively characterise nanoparticulate networks and their clusters to sub-micron sizes.

A close agreement has been established between observable physical and electrical characteristics of these materials. However, the dynamics of how real-world networks operate remains a very open area of research where lots of basic questions remain unanswered.

Contents

List of Figures

List of Tables

Chapter 1 Introduction

This project is concerned with a study of the structural and electrical characteristics of metallurgical grade silicon (mSi) and metal oxide semiconducting nano-structured materials for use in sensor and photovoltaic applications [11–14]. The principal aim of this study is to establish the extent to which Small Angle Light Scattering(SALS) can be combined with Ultra Small Angle X-Ray Scattering(USAXS). This is done in order to explain the electronic and electrical behaviour of metallurgical silicon and other semiconducting nano-structured materials. The local microstructures of the clusters of well-defined silicon nanoparticles and the topology of the network formed from these clusters in printed nano-structured composites have been consolidated with the observed electrical and electronic properties of the materials. This has been achieved in this case by applying the percolation theory [15, 16] and the scaling laws [17, 18] to obtain quantitative correlations of the network topologies and the local micro-structures with the electronic and electrical properties of the studied materials.

An inhouse Small Angle Light Scattering developed in the framework of this research was used to determine the topology of the clusters of particles. The scattering data from this inhouse experiment was then combined with USAXS data to increase the sensitivity of the technique towards lower q-range. Therefore, the main technique used for the direct determination of the actual network topology and the local microstructures of the nano-structured particle networks was an inhouse-built SALS experiment combined with the USAXS and supported by the Scanning Electron Microscopy(SEM). This way, the mesoscale structure of printed layers was observed and characterised and thereafter correlated with the voltage against current (VI) measurements to understand

the topology of the active pathways of the semiconducting nano-structured composites. These could then be used to predict, and ultimately design the electronic properties of the printed layers.

It is envisaged that this study will immensely contribute towards exploiting various physical (e.g. surface and bulk) properties of nano-structured materials for use in sensor and photovoltaic applications. Particular emphasis will be given to the structure, morphology and composition of the metallurgical silicon nanoparticles, which are produced by mechanical attrition of bulk 2503 grade metallurgical grade silicon due to their prevalence in printed electronic inks [19–21]. Silica, alumina, and titania particles will also be studied for comparison purposes.

There are seven chapters in this report, namely, introduction, theoretical background, scattering theory, experimental techniques, results, discussion and conclusion. The *introduction* sets the context and framework for the rest of the thesis and includes a broad overview of printed electronics as applied to either photovoltaics or sensors. The theoretical background chapter addresses the "top-down" and "bottom-up" synthesis of nanoparticles, fractal networks, scaling laws and the charge transport mechanisms in these particle systems. The chapter also addresses charge transport mechanisms in particle systems particularly with regard to the prediction of electronic and physical properties from the newly developed structural models. The *Small Angle Scattering(SAS) theory* chapter discusses theories of small angle scattering, starting with established models such as Guinier's law and Porod's law, leading through fractal power laws and polydispersivity models to the latest fractal scaling models as applied to such systems as those studied.

The *experimental techniques* chapter covers the relevant theories and procedures applicable to SALS and USAXS as well as the applicable analytical techniques. The SEM and voltage against current measurement techniques will also be discussed. The structural and electrical characterisation results will be presented in the *results* chapter and analysed in the *discussion* chapter and finally, the main outcomes of this study will be outlined in the *conclusions* chapter. In order to avoid confusion with the numbering system, the reader is asked to bear in mind that it will be specified whether a graphic is either a formula, figure or table before each number.

Chapter 2 Theoretical Background

This chapter explores the "top-down" and "bottom-up" production of nanoparticles and explains their physical and electrical characteristics. The chapter also addresses ways in which nanoparticles tend to cluster together into larger structures known as *aggregates* and *agglomerates*. A concept of fractals is then used to explain and characterise their physical properties, while *percolation* is used to characterise charge transport on these disordered systems.

2.1 "Top-down" and "bottom-up" production of nanoparticles

There are two general ways of producing nano-structured materials, namely:- the "top-down" and the "bottom-up" approaches [22–24]. The "bottom-up" approach is brought about by the assembly of atoms, molecules or nano scale structures as indicated in figure 2.1($a \rightarrow c$), whereas the "top-down" production of nanoparticles involves size reduction processes, whereby bulk solid materials are reduced to nano-scale dimensions as shown in figure 2.1($e \rightarrow c$) [12, 25].

Isolated and uncontaminated particles are generally produced using bottom-up methods [26]. The techniques includes inert gas condensation, chemical reaction of a precursor [8, 26–28], aerosol synthesis [29], liquid phase methods, self-assembly and positional assembly [25].

The "top-down" approach can be achieved through manipulation of nanometre-sized

materials [30] or breaking down bulk materials into nanoparticles through milling [3,31,32], pyrolysis [19,33,34], evaporation of bulk silicon in an inert atmosphere [35,36], laser induced ablation, lithographic process and chemical reduction [25]. The microstructure, morphology, size distribution and level of contamination of the resulting nanomaterial are dependent on the production method [1, 32].

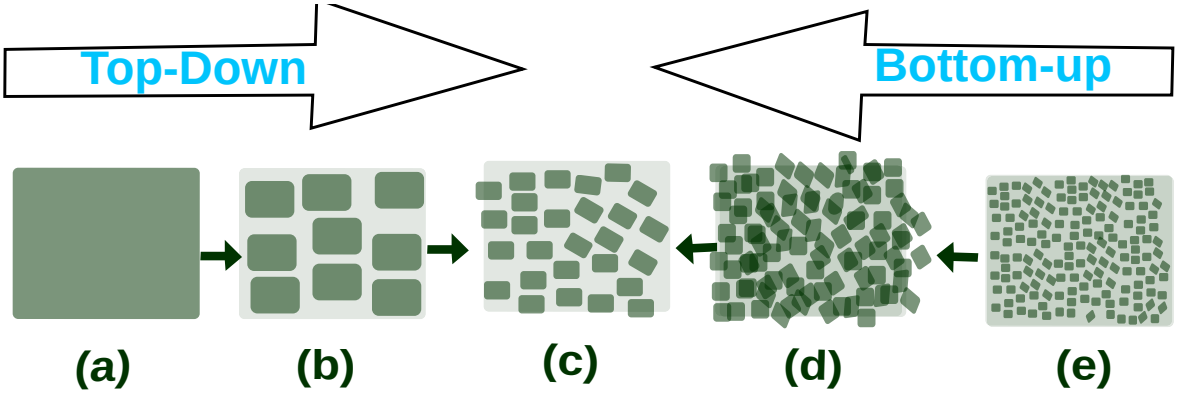

Figure 2.1: *The "top-down" and "bottom-up" production of nanoparticles. (a) bulk material , (b) powder, (c) nanoparticles, (d) clusters and (e) atoms*

In this research, silicon nanoparticles were produced through the "top-down" processes, which involved physical reduction of bulk 2503 metallurgical grade silicon (mSi) through milling. Silica sand was also milled in the same way to produce SiO_2 nano particles. During the milling process, the bulk material was comminuted through brittle fracture and plastic deformation as will be explained further in section 4.1.1 on p26 [3]. The microstructure of milled powder depends on the density of the milling medium, the milling time and the milling medium to powder ratio [32]. This technique is known to yield primary particle sizes of about ± 80 nm [2, 32].

2.2 Fractal networks and scaling laws

2.2.1 Agglomeration and aggregation of nanoparticles

Almost all nanoparticles generally have a tendency to assemble into large structures known as clusters [37, 38]. There are two terms that are often used to describe particle clusters, namely :- *aggregates* and *agglomerates*. These two terms are often used inconsistently and interchangeably [39]. The following definition by Gerstner [40], which has

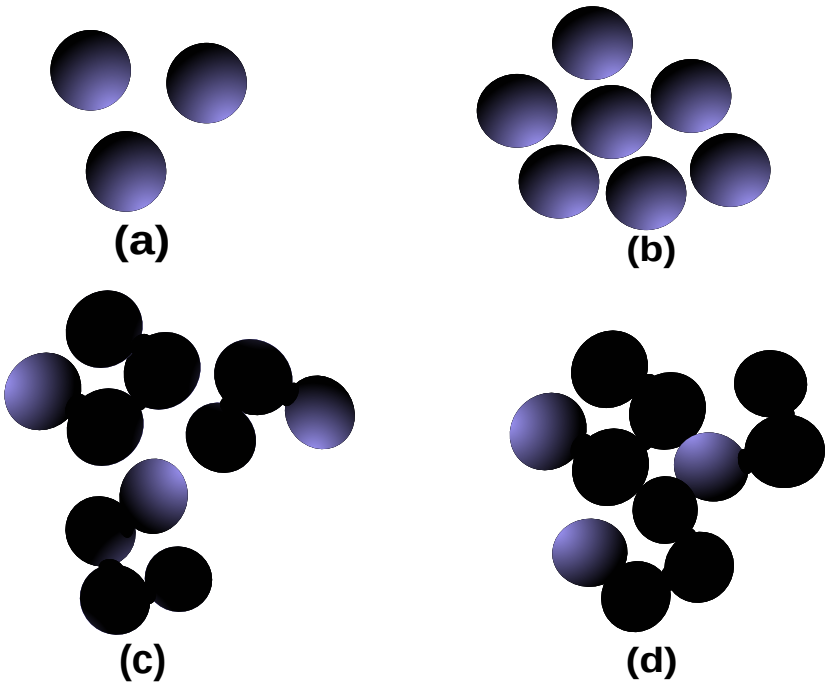

Figure 2.2: *Schematic illustration of aggregation and agglomeration of nanoparticles (a) discrete primary particles, (b) agglomerates of primary particles, (c) aggregates of primary particles, (d) agglomerates of aggregates*

been adopted by the ISO, will be used in this thesis. In an *agglomerate*, the particles, (or clusters of particles) are held together by weak forces, such as the van der Waals forces, and *aggregates* are held together by strong bonds between them [40].

Because aggregated particles such as those illustrated in figure 2.2(c) are strongly attached to one another, the surface of an aggregate is smaller than the sum of the surfaces of the discrete primary particles. The inner surface of an aggregate is inaccessible or partially inaccessible and particles are not readily dispersed. Just like primary particles, aggregated nanoparticles may form agglomerates as illustrated in figure 2.2(d).

Aggregation of particles can be dominated by one of two rate limiting steps, leading to two different types of aggregation, namely; diffusion-limited aggregation (DLA) and reaction-limited aggregation (RLA) [41]. In DLA, the aggregation is very rapid, and the rate is limited solely by the time taken for collisions to occur via Brownian diffusion [42]. In the RLA regime, the rate is limited by the low probability of actually forming a bond upon collision. The occurrence of either of these regimes depends on the height of the potential barrier caused by the repulsive coulomb interaction between

approaching colloid particles. When there is no repulsive barrier (e.g. if the particles have no surface charge), DLA results but when the surface charge is reduced, RLA may occur [42]. Figure 2.3 illustrates the main features of an aggregate of similar primary particles in two dimensions.

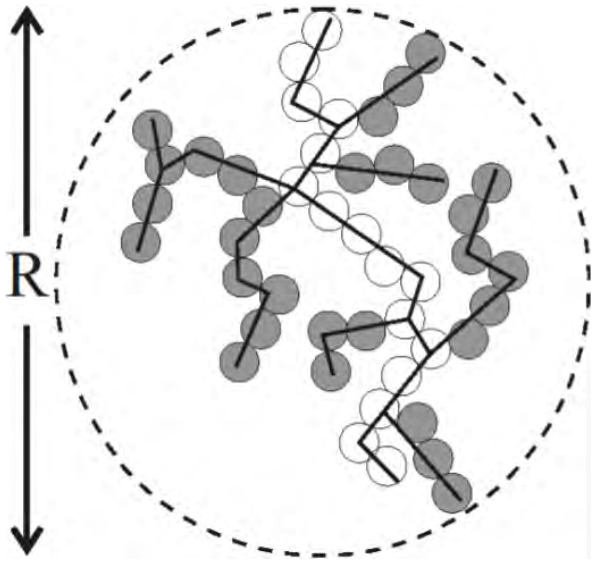

Figure 2.3: *A schematic illustration of aggregate structures in two dimensions [1, 5]*

The number of particles in an aggregate z is known as the degree of aggregation or mass of the aggregate. The minimum connection path d_{min} describes how tortuous or convoluted the aggregate structure is. The fractal dimension d_f is directly proportional to the minimum path d_{min}. This average minimum connection path d_{min} is shown by open circles in figure 2.3 and has p number of primary particles that spans the width of an aggregate of fractal dimension d_f [5]. The fractal dimension d_f is proportional to the average minimum connection path d_{min} according to

$$\frac{d_f}{d_{min}} = c, \tag{2.1}$$

where the proportionality constant c is known as the connectivity dimension (or *intrinsic dimension*). For linear chains, $c = 1$ and $d_{min} = d_f$. *"Regular objects"* such as rods, disks or spheres are defined by a minimum path of $d_{min} = 1$ and therefore $c = d_f$ [43]. The straight lines in figure 2.3 represent the connectivity path of the aggregate with a fractal dimension $d_f = c$ [5]. The branch fraction of the aggregate ϕ_{Br}, which is the fraction of the total number particles that are not included in the minimum path, can be obtained from equation 2.2 [5, 41, 44].

$$\phi_{br} = \frac{z-p}{z} = 1 - z^{\frac{1}{c}-1} \tag{2.2}$$

Particles in an aggregate are typically non-spherical and can have a complex structure. Characterizing these complex structures is often difficult since they typically display disordered and irregular features in three dimensions. Therefore, a concept of fractals is often used to describe them.

2.2.2 Fractal geometry and the scaling theory

The term *"fractal"* was first explained by a Polish-born French mathematician Mandelbrot (1924-2010) in 1982. The term comes from the Latin word *"fractus"* which is derived from *"frangere"*, meaning "to break" or "to form" irregular fragments [45]. A fractal can be created by taking a smooth looking shape and breaking it into self-similar pieces over and over again (e.g. dividing a triangle into four smaller triangles and repeating this process over and over again for each newly formed triangle) [46]. Fractals have a characteristic symmetry of invariance under dilation. Therefore, every piece holds the key to the whole structure [46]. For example, an object with dimension (d) can be divided into N identical parts scaled by a factor r as

$$Nr^d = 1. \tag{2.3}$$

Until the 1970's, classical mathematics was only suited for regular structures, such as lines, squares, rectangles, circles and spheres. Euclidean dimensions can be represented as integers, such as $d = 0$ for the point as , $d = 1$ for a line as in figure 2.4(a) , $d = 2$ for a surface as in figure 2.4(b), and $d = 3$ for a volume as in figure 2.4(c).

Fractals have real and non-integer dimensions (d_f), which are comparable to the equivalent euclidean dimension. For example, the fractal dimensions of shapes shown in figures 2.4(d), (e) and (f) are $1 > d_f > 2$, $2 > d_f > 3$ and $3 > d_f > 4$ respectively and these fractal dimensions can be used to characterize structural irregularities of solid materials [42, 47, 48]. For example, considering an aggregate of z primary particles, a fractal dimension d_f, can be used to provide information about the arrangement of these particles in a cluster. For example, when $3 > d_f > 4$, this implies that the particle arrangements form a compact structure-mass fractal, when $d_f < 2$, particle

are arranged in an open chain-like network and when $3 > d_f > 2$, a two-dimensional projection of the surface of the layer is implied.

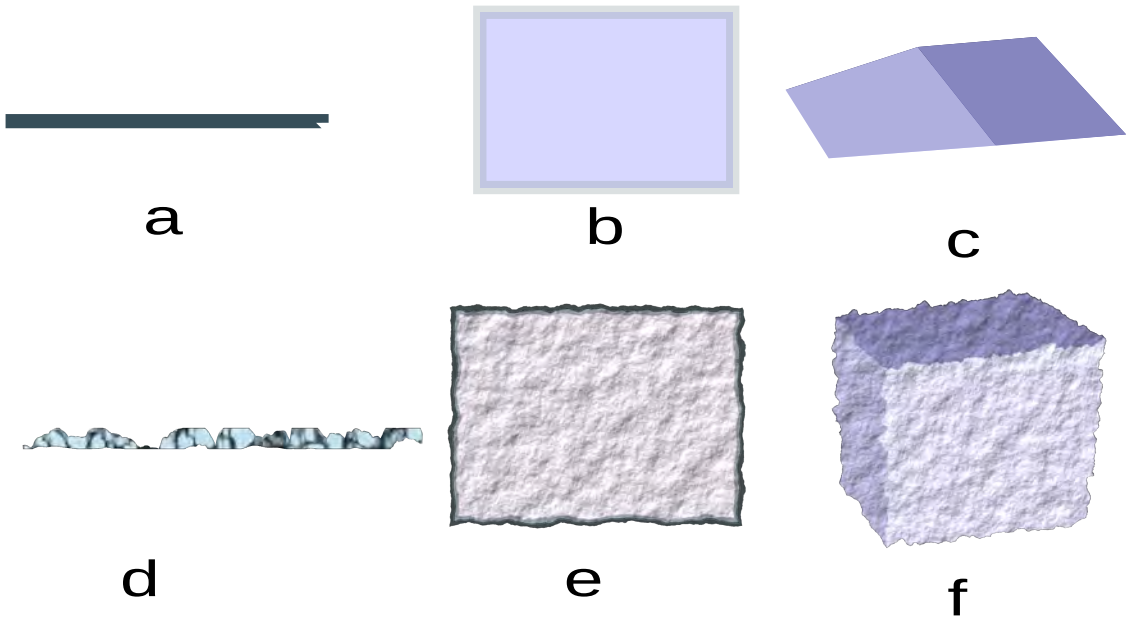

Figure 2.4: *Schematic illustration of different spatial dimensions where a) is a smooth line, b) a smooth surface, c) smooth volume, d) is a rough line, e) rough surface and f) is a rough volume.*

A fractal dimension (d_f) is a measure of the degree of irregularity of the object, which can be achieved through scaling theories. There are various scaling theories that can be used to understand disordered structures. These theories rely on the averageness of the physical or mathematical quantities associated with the random physical structures and attempt to explain the branching or network characteristics [5].

2.2.3 Power laws

The assumption that aggregates have a fractal-like structure, suggests that a power-law relationship exists between the characteristic *euclidean dimension* (e.g. length) and a particular physical characteristic (e.g. mass, volume and surface area) of such aggregates exists [49]. Measurements of these entities are usually expressed as a comparison of that entity with another entity of the same type, called a unit. Therefore, a measurement of an entity G can be expressed as :

$$G = T(G).U(G) \tag{2.4}$$

T(G) being the measure of G and $U(G)$ the unit of G. For example, if G is the length,

$U(G)$ is the standard meter, and $T(G)$ is the number of standard meters with the same length as G [50]. In addition, the entity G has a dimensional symbol, which combines the fundamental units that comprise the entity. For example, volume generally has a dimensional symbol l^3 (i.e. $V \propto l^3$), surface area $V \propto l^2$ and surface area to volume $S/A \propto l^{-1}$. In this way, the mass of an object with uniform density ρ would scale as $m \propto l^3$, since mass can be expressed as a function of volume (i.e. $m = \rho V$).

Two types of fractals are usually observed in nanoparticle clusters, namely the mass fractals(M) and surface fractals (S). Surface fractals are structures whose surfaces (not mass or volume) are characterised by fractal properties, whereas mass fractals are substances or structures whose mass and surface are characterised by fractal properties, and they often are aggregates of subunits [47]. For a fractal system formed by the aggregation of primary particles in a self-similar geometrical arrangement, the mass or surface of the system increases with its linear dimension l according to

$$M \propto l^{d_m}$$

or

$$S \propto l^{d_S}$$

where d_M and d_S are the surface and mass fractal dimensions respectively, with non-integer values between 1 and the *Euclidean dimension* d [17, 51, 52].

2.3 Charge transport in particle systems

Charge transport in inhomogeneous conductors can be understood by studying how particles are connected [15, 16]. Percolation theory can explain the origin of connected clusters on a networked system [53]. The theory provides a quantitative description of the connections in a network [53–56]. The two most common statistical assumptions of this model are *site percolation* and *bond percolation* [29]. The major practical focus of percolation studies has been the search for the *percolation threshold*, which is the minimum filler concentration necessary to create a continuous network that covers the entire system [15].

In the early 1940s, an American chemist and Nobel laureate, Paul Flory (1910-1985)

first explored the idea of percolation in a study of gelation in polymers [54]. In 1957, Broadbent and Hammersley introduced percolation modelling while studying a distribution of the fluid on a porous medium and were able to quantify how a fluid randomly spread through a medium by associating the random process with the medium, rather than with the fluid, i.e. percolation instead of diffusion [16].

In site percolation models when the concentration of allowed sites x is much less than the threshold concentration (i.e. $x << x_c$), the allowed sites appear isolated or in small clusters. As x increases, larger clusters start to emerge as the mean size of clusters also increases. As $x \to x_c$, the large clusters start to merge until finally, only one large cluster, the infinite cluster, exists as $x > x_c$. Correspondingly, the ratio of the number of occupied sites N in this infinite cluster ($N \to \infty$) to the total number of available sites known as the *site percolation probability* $P^{(s)}$, rises sharply when $x >> x_c$ [55]. In an electrical network, this is the fraction of the volume where DC conduction is possible [16]. $P^{(s)}$ near the threshold can be represented as a power law

$$P^{(s)} \approx (x - x_c)^s, \tag{2.5}$$

where $0.3 \leq s \leq 0.4$ and $s = ds - 1$. The specular dimension ds in this case is equal to the connectivity dimension c from equation 2.1 above [56, 57]. A random network of particles can be increased by either adding more nodes to the network or by increasing the number of links within an existing network. By gradually increasing the link probability parameter, critical thresholds and phase transitions may occur [56, 58]. These thresholds separate regions where percolation does and does not occur. In reciprocal space, percolation does not occur when the percolation probability, also known as the infinite cluster density is zero (i.e. $P^{(s)} \approx P_\infty(p) = 0$).

The first threshold is usually when the average connection degree exceeds the total number of nodes in a network. At this threshold a connection between the network nodes is apparent. When the connection degree reaches unity (i.e. when every node has on average one connection), the network starts to appear connected and giant components start to emerge within the network (i.e. one dominant cluster). At this stage, cycles also start to appear due to feedback loops on the network. Another threshold occurs when nodes have an average degree of $\log N$, where everything starts to be con-

nected (i.e. there is typically a path to all other nodes in a network) [55].

Real world networks are dynamic in nature due to resource constraints. The network connection is always a function of the resource constraints. This often results in preferential attachments between the nodes, which lead to cluster formation [55]. These constraints are not usually evenly distributed and the network topology often reflects this [59]. It is therefore necessary to know the attributes of nodes within a network (e.g. material type) since connections are based upon them. It is necessary to know the probability of nodes of the same kind connecting with one another other compared to that of nodes of different types to connect with one another. The results of considering these factors provides a much more realistic model, where local clustering and some distance relations can be explored fully. Underlying this relatively abstract model of network development, is a much more complex set of questions about the local insensitivity of the nodes in a network. The dynamics of how real-world networks behave remains a very open area of research where many basic questions remain unanswered.

Chapter

3 Small Angle Scattering

This chapter covers the theoretical and historical background of Small Angle Scattering (SAS) with special focus on Small Angle Light Scattering (SALS) and Ultra-Small Angle X-ray Scattering (USAXS). The chapter will first establish fundamental concepts of SAS in section 3.1, which includes the scattering density, scattering cross section, form factor and structure factor. Thereafter, various scattering laws such as Guinier's law and Porod's law will also be discussed, leading through fractal power laws and polydispersivity models to the latest fractal scaling models as applied to such systems as those studied. Information on particle shapes and dimensions is mixed in the scattering function, therefore, assumptions of particle shapes or size distributions must be made for analysis purposes. These assumptions will be made looking at the Scanning Electron Microscopy (SEM) in section 5.2 on page 56. Therefore, for the discussion of the basic principles in this chapter will use examples of spherical and ellipsoid scatterers will be used throughout.

3.1 Scattering theory

The pioneers of SAS were Debye [60,61] , Guinier [62], Porod [63,64] and Kratky [65–68] who contributed immensely to developing the theories and techniques involved. This section, will only focus on elastic scattering of x-rays and visible light by a medium of disordered nano-particulate systems in the micron to nano size ranges to provide information about sizes, shapes and orientation of constituent particles. SAS originates from characteristic inhomogeneity in a medium through which light is travelling [69–71].

Different scattering techniques can therefore be employed to characterise these inhomogeneities. Static Light Scattering (SLS) is an optical technique that measures the intensity of the scattered light as a function of the scattering angle to obtain information about stationary scattering [72]. SAS techniques can cover an angular range of up to 1^o with the SAXS regime usually covering length scales of $\approx$ 15 - 20 Å ($q \approx 0.3\text{Å}^{-1}$).

In SALS, laser light is scattered mostly by dielectrics (non-conductors), whereas x-rays and thermal neutrons are scattered mostly by electrons and nuclei respectively [73]. In SALS, incident laser light causes forced oscillating dipoles, which in turn emit light (of the same wavelength as the incident beam) in all directions. Unlike USAXS, SALS relies on polarisability contrast instead of the electron density contrast [7]. Because of the different wavelength ranges of x-rays and visible light, USAXS is not sensitive to electron density fluctuation on atomic scales but can explore dimensions of a few nanometres, whereas SALS can only map variations on sub-micron to micron-size scales [70]. However, taken together, a combination of SALS and USAXS can present a full spectrum of structural characterisation of nano-structured materials from primary particles through aggregates and agglomerates, and in turn to their clusters in sizes ranging from nano to micron ranges.

The scattering principles of these techniques are illustrated in figures 3.1, 3.2 and 3.3. Figure 3.1 shows an incident plane wave(ψ_i) with momentum k_i that is elastically scattered into a spherical wave(ψ_s) with momentum k_s by a particle. In this case, both momentum and kinetic energy are conserved and therefore $|k_i| = |k_s|$ when observed from the centre of mass [74]. However, the directional change from incident $\vec{k_i}$ to the scattered $\vec{k_s}$ waves is defined by a scattering vector $\vec{q} = \vec{k_s} - \vec{k_i}$. The incident and scattered waves may be expressed by the relations 3.1 and 3.2 respectively,

$$\psi_i \propto e^{ik_i.r} \tag{3.1}$$

$$\psi_f \propto A(q)\frac{e^{ik_s.r}}{r} \tag{3.2}$$

where $\vec{k_i}.\vec{k_s} = \cos\theta$ and the time independent wave function outside the interaction region can be expressed using equation 3.3.

$$\psi \propto e^{ik_i.r} + A(q)e^{ik_s.r} \tag{3.3}$$

The schematic in figure 3.1 illustrates a principle of scattering scattering using a single scatterer.

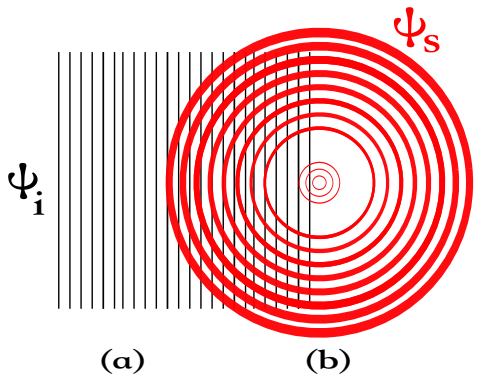

Figure 3.1: *A schematic illustration of a scattering principle where (a) an incident plane wave (ψ_i) is scattered by a single particle into (b) outgoing spherical waves (ψ_s) [6].*

where $A(q)$ is the scattering amplitude [74]. Figure 3.2 illustrates the scattering process for two spherical scatterers, which are a distance r apart and located at positions x and y respectively.

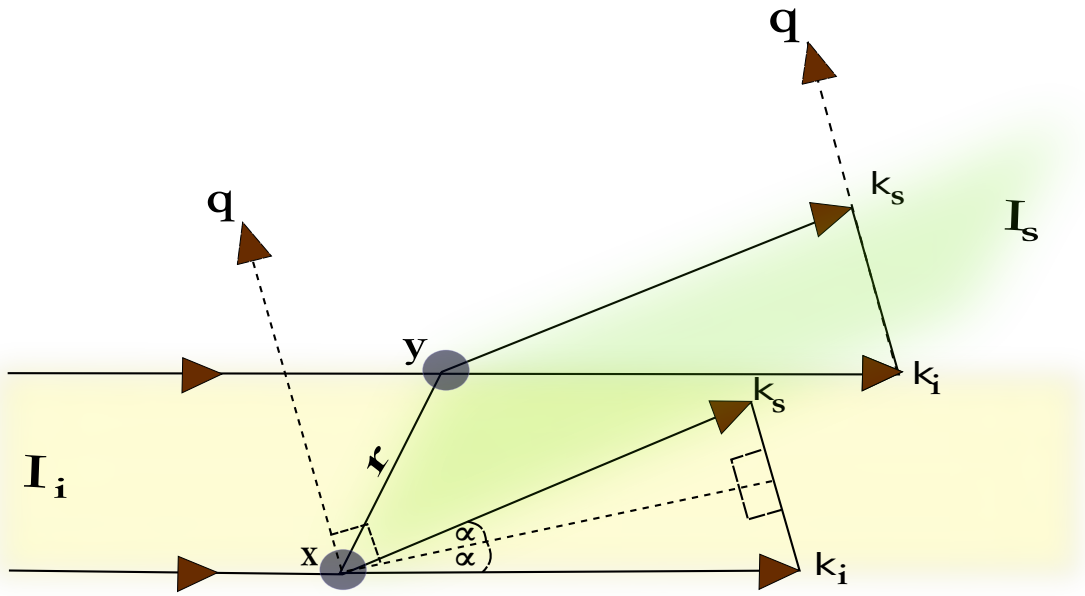

Figure 3.2: *A schematic illustration of scattering by two particles [7].*

I_i and I_s are intensities of the incident and scattered waves respectively. The scattered waves can each be represented as $e^{i\phi}$, where ϕ is the phase relationship. The phase

relation between scattered waves at x and y is given by

$$\phi = -qr, \tag{3.4}$$

and since

$$k_s - k_i = 2\sin\frac{\theta}{2}, \tag{3.5}$$

and the magnitude of the scattering vector q is given by

$$q = \frac{4\pi}{\lambda}\sin\frac{\theta}{2}. \tag{3.6}$$

Therefore, the phase relation ϕ can be expressed by combining equation 3.4 and 3.6 as follows : -

$$\phi = \frac{2\pi}{\lambda}(k_s - k_i)(-r). \tag{3.7}$$

3.1.1 Scattering density $\rho(r)$

A scattering length b_i (also known as scattering contrast) characterizes the local interaction of radiation with materials. The scattering density is given by

$$\rho(r) = \sum \rho_i(r) b_i \tag{3.8}$$

where $\rho_i(r)$ is the local density of the scatterers of type i. The correlation between positions and orientations of particles increases with the concentration of scatterers [75]. Generally, the structural inhomogeneity of the medium surrounding a particulate system is essentially smaller in size compared to the particle structure inhomogeneity. In this way, the excess scattering *g(r)* in the case of mono-disperse systems can be obtained by merely subtracting the non-zero value of the scattering density of the medium ρ_s from the scattering density of the particle $\rho(r)$. Therefore, since the sample volume is much greater than the particle volume V, the contrast $\Delta\rho$ can be expressed as the difference between the mean particle intensity and the medium density, as

$$\Delta\rho = \langle g(r)\rangle = V^{-1}\int_V \big[\rho(r) - \rho_s\big]dr = \rho - \rho_s. \tag{3.9}$$

If the scattered waves from a large collection of dielectric (non-conducting) scatterers

are coherent in nature (i.e the phases of a waves are conserved after scattering), their intensities can be found by taking the absolute square of the sum of their amplitudes [76]. Therefore, a dimensionless scattering amplitude of a unit volume dV of a collection of these scatterers is an integral sum of the amplitudes of all secondary waves. The scattering amplitude can be expressed as a function of the scattering density.

$$A(q) = \int_V \rho(r) e^{iqr} dV. \tag{3.10}$$

Multiplying equation 3.10 by its complex conjugate A^* yields

$$AA^* = \int \int \rho(r_1)\rho(r_1) e^{iq(r_1 - r2)} dV_1 dV_2 \tag{3.11}$$

which can then be split into the auto-correlation function $\rho^{-2}(r)$ and the intensity function $I(q)$ in 3.12 and 3.13 respectively.

$$\rho^{-2}(r) = \int \rho(r_1)\rho(r_1) dV \tag{3.12}$$

$$I(q) = \int \rho^{-2}(r) e^{iqr} dV \tag{3.13}$$

The exponential function in equation 3.13 may be replaced by its average over all directions of r according to the Debye formula [61, 77]

$$< e^{iqr} >= \frac{sin(qr)}{qr}. \tag{3.14}$$

3.1.2 Scattering cross section (σ)

An effective area that quantifies the intrinsic likelihood of a scattering event is known as the *scattering cross section* (σ). This is illustrated in figure 3.3,

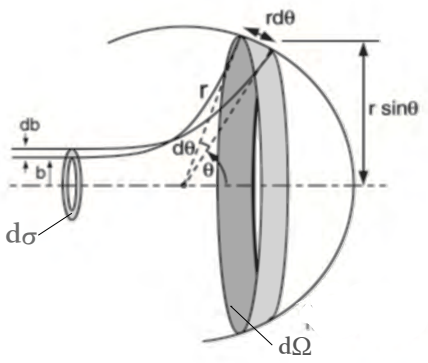

Figure 3.3: *A schematic demonstration of the scattering cross section and solid angle [7]*

The square of the scattering amplitude is equal to the differential cross section $\delta\sigma$ over the scattering solid angle according to

$$\left|A(q)\right|^2 = \frac{d\sigma}{d\Omega}$$

and therefore, the differential cross section $\delta\sigma$ may be expressed as

$$d\sigma = \left|A(q)\right|^2 d\Omega \tag{3.15}$$

A scattering cross section depends sensitively on the energy of the incoming radiation [78]. During elastic scattering ($\sigma_{elastic}$), the internal energies remain constant and no further particles are created or annihilated. The total cross section can be obtained by integrating over all solid angles (Ω),

$$\sigma = \int \frac{d\sigma}{d\Omega} d\Omega = \int_0^{2\pi} d\phi \int_o^{\pi} \sin\theta \frac{d\sigma}{d\Omega} \tag{3.16}$$

where the differential cross section $d\sigma/d\Omega$ is the ratio of the number of quanta scattered into direction (θ, ϕ) per unit time per unit solid angle N, divided by incident flux j_i [7]. For a solid impenetrable sphere in figure 3.4, the differential cross section can be obtained as

$$\frac{d\sigma}{d\Omega} = \frac{N}{j_i} = \frac{b}{\sin\theta}\left|\frac{db}{d\theta}\right| = \frac{R^2}{4} = \frac{d\sigma_0}{d\Omega} S(q) \tag{3.17}$$

where $S(q)$ is the structure factor defined in equation 3.18. It is necessary to model the scattered intensity by calculating the form and structure factors so as to obtain information from systems of interacting particle systems.

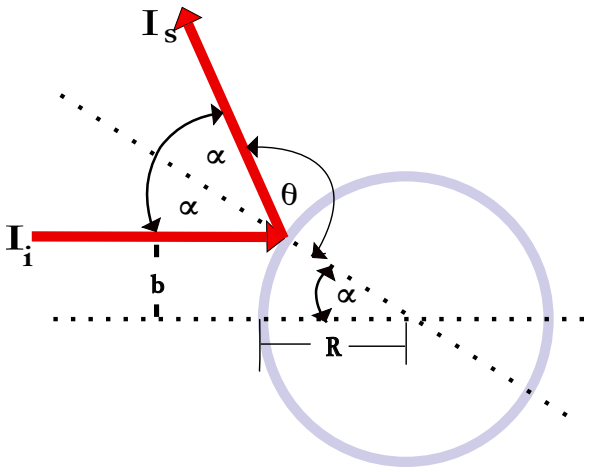

Figure 3.4: *Light reflection by a solid impenetrable sphere with radius R*

3.1.3 Structure factor $S(q)$

The structure factor $S(q)$ is a mathematical function that describes the inter-particle interference of the scattered light by an arrangement of scatterers and how this influences the overall scattered intensity [72, 79]. A detailed analysis of the structure factor $S(q)$, can provide information about the nature of interaction potentials. S(q) provides information about the intra-particle interactions and is defined as :-

$$\langle S(q)\rangle = S(q) = 1 + n_p \int_0^\infty 4\pi r^2 [g(r) - 1] \frac{\sin qr}{qr} dr \tag{3.18}$$

where r is the distance from a reference point and $g(r)$ is the pair *distance function*. In the case of an isotropic system of spherical scatterers, the average structure can be calculated around a centrally-located sphere. Mutual interferences must also be considered in the case of *aggregation of particles* [66]. Therefore, light scattering may serve not only to determine the shape and properties of the isolated particles but also to obtain valuable data on the nature of inter-particle interactions existing in a condensed medium, which is the case in this research.

3.1.4 Form factor

The form factor $F(q)$ is a mathematical function that can be used to calculate shape irregularities. $F(q)$ depends only on the shape of the particles and can be expressed as

$$F(q) = \left[\int_0^\infty r^2 g(r) \frac{\sin qr}{qr} dr \right]^2 . \tag{3.19}$$

By expanding in $sin(qr)/(qr)$ series the term the Guinier approximation for the form factor is obtained as

$$F(q) \simeq 1 - \frac{(qR_g)^2}{3}, \tag{3.20}$$

where the (optical) radius of gyration is defined as

$$R_g^2 = \int_0^\infty r^2 g(r) dr. \tag{3.21}$$

The importance of such an approximation lies in the fact that it allows for determination of R_g by performing a simple linear fit to the Guinier plot (i.e a plot $I(q)$ vs. q^2) for scattering from spherical particles that shows that the form factor attains a plateau at a value of $qR = 1$ and for $q << 1$, whereas if $qR >> 1$, the form factor is affected by the inter-particle interference effects.

3.1.5 Scattering intensity $I(q)$

A study of disordered materials by diffraction methods involves measuring the scattering intensity, which is a function of the microscopic state of the system [80]. The scattering intensity for a non-correlated system can be expressed as follows :-

$$I(q) = F(q) * S(q) \tag{3.22}$$

where $I(q)$ is the experimental intensity, $F(q)$ is the form factor of the particles that describes intra-particle interactions (i.e size and shape) and $S(q)$ is the structure factor of the solution describing inter-particle interactions (i.e. whether repulsion or attraction). For a correlated system, equation 3.22 can be expressed as

$$I(q) = AF(q)^2 S(q) \tag{3.23}$$

Assuming spherically or nearly spherically symmetrical scattering amplitudes, the average scattering intensities *I(q)* can be described as a function of the average contributions of the individual particles

$$I(q) = \langle N \rangle \left\{ 1 - \frac{1}{v_1} \int_o^\infty [1 - F(r)] \frac{\sin qr}{qr} 4\pi r^2 dr \right\}. \tag{3.24}$$

where N is the number of particles and v_1 is the mean sample volume per particle. Equation 3.24 expresses the scattering intensity as a function of the form factor $F(r)$ of the scattering particles.

The scattered light intensity I(q) contains correlated physical characteristics of the scatterers. The scattering intensity $I(q)$ can be calculated from the square of the scattering amplitudes as

$$I(q) = \Big\langle A(q) \Big\rangle^2 \tag{3.25}$$

where the scattering amplitude $A(q)$ can be described using the scattering potential and the scattering length density according to

$$A(q) = \int \rho(r) e^{iqr} dV. \tag{3.26}$$

For an ellipsoidal particle with semi-major and semi-minor axes a and b, and with constant orientation, the scattered intensity $I(q, a, b)$ can be obtained as

$$I_o(q, a, b) = \Delta\rho^2 \left(\frac{4}{3}\pi a b^2\right)^2 \left(\frac{3\sin x - x\cos x}{x^3}\right)^2, \tag{3.27}$$

where $x = \sqrt{a^2 h_1^2 + b^2 h_2^2}$ with h_1 and h_2 being the perpendicular components of the scattered beam on the detector and $\Delta\rho^2$ is *density difference* between the particle and the surrounding medium. The overall intensity can be obtained by multiplying the function for the scattering of a single particle in equation 3.27 by the distribution of sizes such that

$$I_0(q, a, b) = \int\int D(a, b) I_o(q, a, b) da db, \tag{3.28}$$

where $D(a, b)$ is the function defining the semi-axes of the ellipsoid. For a spherical particle, $a = b$, $I(q, a, b) \Rightarrow I(q, R)$ and $ab^2 = R^3$. Therefore equation 3.27 can be expressed as

$$I_o(q, R) = \Delta\rho^2 \left(\frac{4}{3}\pi R^3\right)^2 \left(3\frac{\sin R - R\cos R}{R^3}\right)^2 \tag{3.29}$$

which indicates that the scattered intensity scales with the sixth power of the radius

$$I(q) \propto R^6. \tag{3.30}$$

Based on this, the scattered intensity of the smaller size particles disappears very rapidly with the decrease in radius of the scattering particles. The scattering function of the mono-dispersed spherical scatterers is the summation of the individual scattering functions of the individual spheres

$$I(q,R) = \sum R^6 P(R) dR. \tag{3.31}$$

The scattering patterns of different sizes of spheres will show maxima in different regions of the scattering curve. The maximum fractional contribution of a single particle scattering function on the total scattering function is known as the *observability* [78]. When observability is plotted against the radius of the spheres, a distinct bend occurs around π/q_{max}, below which, observability scales with R^6 and above that, it scales with R^2. Therefore, within a q-range limit, observability scales with R^2 while intensity scales with R^6 as shown below by equations 3.32 and 3.33.

$$I(q,R) = \sum R^2.R^4 P(R) dR, \tag{3.32}$$

and

$$I(q,R) = \sum R^2 P^*(R) dR. \tag{3.33}$$

This can therefore be translated in to a relative number of particles required to see any effects of these particles in the scattering pattern. The scattering curve of a diluted system of similar particle sizes can be approximated by

$$I(q) \propto e^{-aR_g^2 q^2}, \tag{3.34}$$

where a is the factor depending on the orientation of the particles and R_g is known as the radius of gyration

$$R_g^2 = \frac{\int \triangle\rho(r_1) r_i^2 dV_i}{\int \triangle\rho(r_i) dV_i} \tag{3.35}$$

for a sphere $R_g = R\sqrt{\frac{3}{5}}$ and. For randomly oriented particles, $a = 1/3$ hence

$$I(q) = I_0 e^{-\frac{1}{3}R_g^2 q^2}. \tag{3.36}$$

3.2 Scaling laws

There are two basic approximations that are generally used for analysing the small angle scattering data, namely:- Guinier's and Porod's laws. The Porod law is used for regions where $q > 1/r$ and Guinier law for regions where $q \leq 1/r$. A unified Guinier/Power-law is a combination of both the Guinier and Porod laws. These three will be discussed in the following sub-sections.

3.2.1 Guinier's law

Guinier's law is widely used to determine basic molecular parameters such as radius of gyration(R_g) and molecular weight (M_w) [81]. In the low q regime, as $q \to 0$, intensity can be approximated by

$$I(q) = I_0 e^{-\frac{1}{3}q^2 R_g^2}, \tag{3.37}$$

$$lnI(q) = -\frac{1}{3}R_g^2 q^2 + lnI_0. \tag{3.38}$$

A graph of $lnI(q)$ against q^2 will yield a straight line with a slope $= -\frac{1}{3}R_g^2$ and intercept at lnI_0. In practice, the Guinier-plot (i.e. $lnI(q)$ v/s q^2) is widely used to determine the radius of gyration. A straight line indicates no aggregation and enables R_g to be determined directly from the slope. If the plot is curved at low q, that implies either attraction or repulsive forces between the particles, and therefore it will not be possible to find R_g from the slope.

3.2.2 Porod's law

At large q, $I(q)$ is inversely proportional to the fourth power of the scattering vector (i.e. $I(q) \propto q^4$) [82–84]. The total small angle scattering from a two phase sample is a constant (e.g. uniform particles in a homogeneous medium) and thus

$$\frac{\pi}{q^*}.\lim_{q\to\infty} I(q).q^4 = \frac{S}{V}. \tag{3.39}$$

where $q^* = q/4\pi$ is the scattering invariant and the surface to volume ratio S/V describes the specific surface of the sample. This law is particularly applicable to systems with sharp interfaces, and is generally used to probe local structures in a

range smaller than the size of the scattering objects. The scattering function can be expressed in terms of the form factor as

$$I(q) = \Delta\rho^2 V^2 f(q), \tag{3.40}$$

where $f(q)$ is the form factor of a single spherical scatterer with volume V and $\Delta\rho$ is the scattering contrast. The scattering law for sharp interfaces is therefore given by

$$I(q) = \frac{\Delta\rho^2 2\pi S}{q^4} \rightarrow I(q) = \frac{I_0}{q^p} \rightarrow \log I(q) = logI_0 - p\log(q), \tag{3.41}$$

where S is the surface area of the sphere. The Porod slope p can be used to provide a fractal dimension ($p = d_s$) of the scattering objects from a plot of $\log I(q)$ vs. $\log q$, at high q. Therefore, a slope of a $\log I(q)$ vs. $\log q$ curve p, can be interpreted using the d_s as explained in section 2.2.2, as follows:-

Slope value(p)	**Implication**
-1	Rigid rods
-2	Gaussian chain in a dilute system
between -3 and -4	rough interface of fractal dimension (d)
-4	smooth interfaces between domains in multi-phase systems

The slope S of a Porod's plot of $q^4 I(q)$ vs. q turn to a plateau (a constant value given by $\Delta\rho^2 2\pi S$ from equation 3.41) [47].

3.2.3 Unified power law

Due to loss of phase information in Guinier's and Porod's laws, they each fall short of extracting the topological features of the scatterers. However, combining them provides a general unified power law equation that can be used to extract the topology of fractal aggregates from a scattering curve with multiple regimes [41].

The Unified power law can be expressed by combining equation 3.37 on p22 and a modified version of the Porod's equation 3.41 to accommodate finite structures as follows:-

$$I(q) \approx Gexp\left(\frac{-q^2R_g^2}{3}\right) + B\left[\frac{\left[erf\left(qR_g/\sqrt{6}\right)\right]^3}{q}\right]^p \tag{3.42}$$

where G is the classic Guinier pre-factor, B is a pre-factor specific to the type of power-law scattering [18, 82]. Equation 3.42 can be used to describe primary particles in an aggregate at the first structural level fitting. For structures with more than one size-scale features, equation 3.42 can be expressed as follows:-

$$I(q) \approx \sum_{i=1}^{n} G_i exp\left(\frac{-q^2R_{g,i}^2}{3}\right) + B_i exp\left(\frac{-q^2R_{g,i+1}}{3}\right) + B\left(\frac{\left[erf\left(qR_g/\sqrt{6}\right)\right]^3}{q}\right)^{p_i}, \tag{3.43}$$

where i represents an individual structural level with its own set of R_g, P, G and B parameters that can be used to define the morphology and dimensions of the scatterers at different length scales. For example, the degree of aggregation z in equation 2.2 on p7 can be found from the Guinier and Porod prefactors in the unified function by

$$z = \frac{G_2}{G_1}, \tag{3.44}$$

and a dimensionless polydispersity index (PDI) can be expressed as

$$PDI = \frac{B_1R_{g,1}^4}{1.62G_1}, \tag{3.45}$$

and the minimum connection path from equation 2.1 [44] as

$$d_{min} = \frac{B_2R_{g,2}^{d_s}}{\Gamma(d_s/2)G_2}. \tag{3.46}$$

Chapter 4 Experimental Techniques

This chapter describes the four types of particles used in this research project; how these particles were used to create the inks listed in table 4.1 on p31; how the inks were used to print samples on flexible substrates; and lastly, how the samples were characterised with respect to their structural and electrical properties.

4.1 Sample preparation

This section presents a short description of the materials used in this research project, where they were sourced and then finally it points out where in the experiments these materials were used. A full procedure of how these materials were used will later be discussed in chapter 5.

Four types of particles were studied in this research, namely:- metallurgical silicon (mSi), silicon dioxide (SiO_2), titanium dioxide (TiO_2) and aluminium dioxide (Al_2O_3). These materials will be referred to in this research project as silicon, silica, titania and alumina respectively. Special interest will, however, be placed on silicon, as it dominates the electronics industry [1, 13]. The silicon and silica particles were milled from bulk materials as explained in section 4.1.1 (p26). Four inks were made and used to print samples, firstly on paper, which is semi-porous and secondly, on non-porous 100 μm polyethylene terephthalate (PET) film substrates. Four sets of printed sheets, consisting of one print from each ink for each set, were chosen at random and taken through the structural and electrical characterisation.

4.1.1 Mechanical milling

Milling was performed using a vibratory disk mill like the one shown in fig. 4.1. This is a high-energy vibratory mill equipped with a four-way adaptor to accommodate four milling vessels shown in fig.4.2b, which uses the pestle to crush the feedstock illustrated schematically in in fig.4.2b a.

Figure 4.1: *A photograph of a laboratory high-energy orbital pulveriser mill*

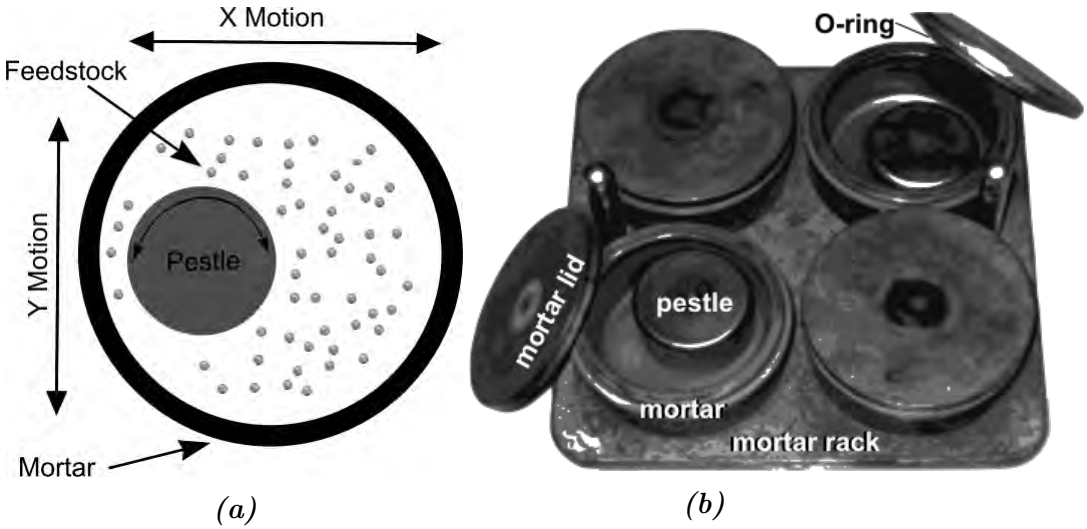

Figure 4.2: *(a) A schematic of the milling process (b) a photograph of the milling equipment [8]*

The mortars had an inner diameter of 8 cm and depth of 3.7 cm. A cylindrical pestle

in figure 4.2b with a diameter of 5.5 cm, height of 3.3 cm and a mass of about 0.6 kg was placed inside the mortars to crush the feedstock during the vibratory motion of the mill. The feedstock for milling silicon particles was a 2503 grade polycrystalline silicon metal, provided by Silicon Smelters (PTY) Ltd, Polokwane, South Africa and the feedstock for silica particles was silica sand.

The mill had to be thoroughly cleaned before particles could be milled. Cleaning was achieved by milling silica sand for 30 minutes followed by a rigorous process of cleaning the mortar, mortar lid, O-ring and pestle shown in figure 4.2b (p26) using paper towels, acetone and methanol. The vessels were closed with lids fitted with rubber O-rings to provide airtight seals. The four milling vessels were then mounted on a four-way adapter and clamped between a rubber pad and a heavy metal plate as shown in figure 4.2b. This process was repeated three times before loading the desired feedstock into the four mortars.

This equipment was used to mill mSi and SiO_2 nanoparticles respectively. In each case, the feedstock was milled for 1 hour and allowed to cool for 30 minutes. Thereafter the pots were de-caked one pot at a time within 5 minutes. The sequence was repeated to mill effectively for five hours [31]. At the end of the milling process, the milling pots were allowed to cool for 1 hour before opening them to harvest the powders. Figure 4.2 shows a schema of the milling process and a photograph of the milling equipment.

The milled powders were harvested directly from the mill in their dry state and stored in airtight plastic containers.

4.1.2 Ink preparation

To attain stable inks, 20 g of particles of metallurgic silicon (mSi), silicon dioxide (SiO_2), titanium dioxide (TiO_2) and aluminium dioxide (Al_2O_3) were each combined with 8.57 g of flexi-clear binder, thereafter mixed with an acrylic flexi-clear binder, which was obtained from Marchem in Cape Town, South Africa. This resulted in a 70:30 particle to binder weight ratio for every ink. The particles were combined with the binder in small quantities at a time followed by thorough mixing for approximately 5 minutes until a uniform paste was formed, followed by adding propan-1,2-diol (propy-

lene glycol) to adjust the viscosity of the paste until it met the rheological requirements for screen printing [3, 31, 85, 86].

Propylene glycol was obtained from Sigma-Aldrich, Steinheim in Germany, and used to thin the ink until it was ready for screen-printing.

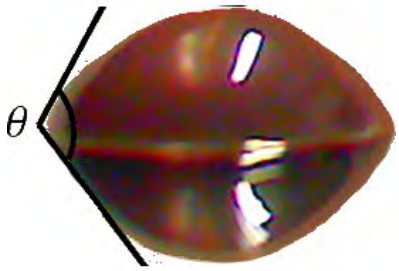

Figure 4.3: *Enlarged image of an ink drop showing the contact angles with glass slide*

The viscosity of the ink was determined by measuring the contact angle of the ink on a glass surface using a contact angle goniometer as shown in figure 4.3 [3, 32].

4.1.3 Sample printing

The nanoparticle-based inks described in section 4.1.2 (p27) were used to print samples onto both plain paper and on PET films substrates using an ATMA AT-60PD semi-automatic flatbed screen printer. The substrates were held in place by a vacuum bed during each print stroke.

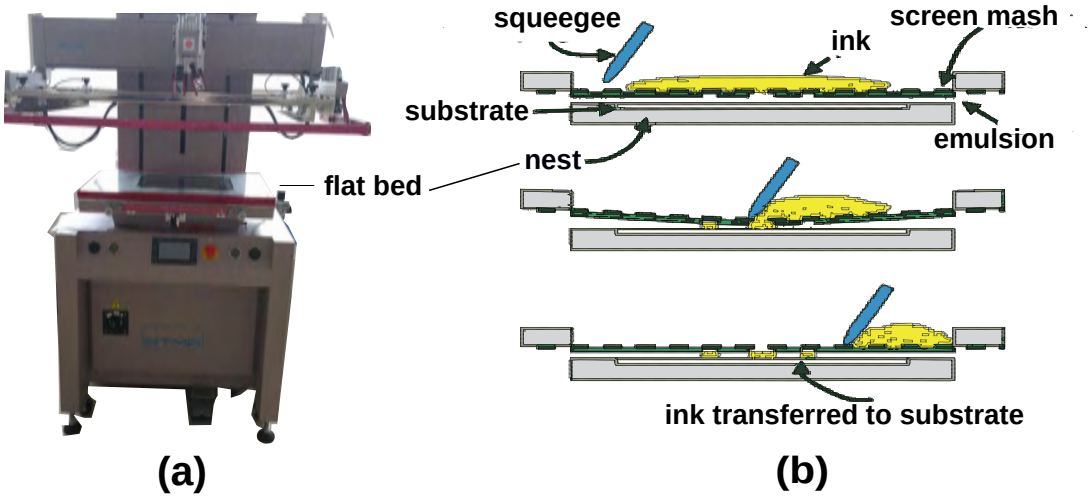

Figure 4.4: *(a) ATMA AT-60PD semi-automatic flat-bed screen printer (b) a schema of the printing process [2]*

The following settings were used on the screen printer, namely:-

- the angle between substrate and screen (i.e. off-set contact) was set to 0^o
- the speed at which the squeegee traversed across the printing screen (i.e. printing speed) was set to 200 mm/s
- the contact angle of squeegee on the printing screen (i.e. squeegee angle) was set to 20^o
- only one printing cycle per substrate was made (i.e. single print stroke)
- the tension of the fibre mash on the screen was measured to be $\pm$ 23 N/cm

The squeegee speed, off-contact and print stroke settings were adjusted digitally while other variables such as squeegee pressure and position of the vacuum table were adjusted manually using micrometre screws. Ten samples were printed on each substrate sheet (see figure 4.6, p30) and multiple sheets were printed using each ink. A stencil, which was made of a 40 μm diameter stretched sefar monofilament polyester fibre

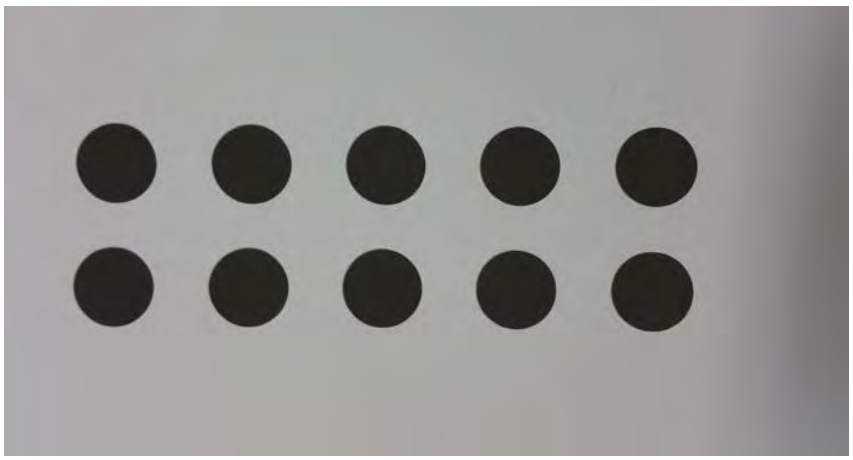

(a) *Printed samples without silver contacts*

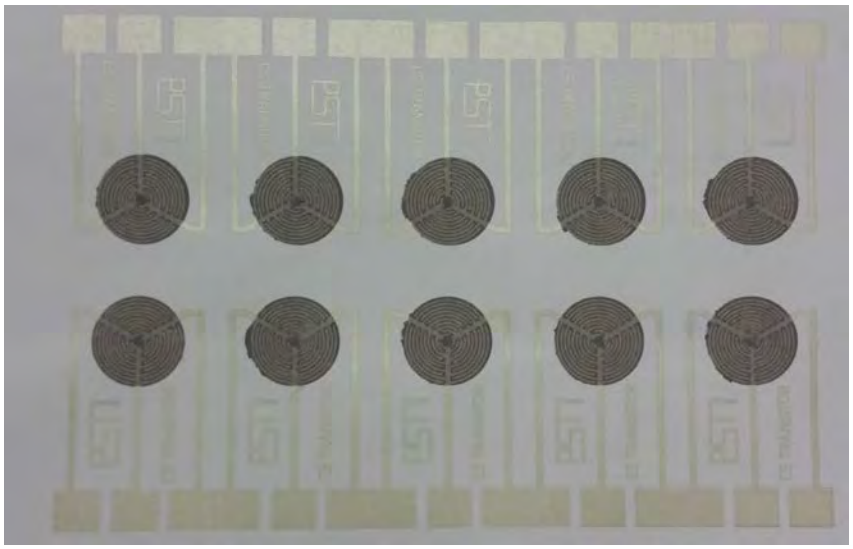

(b) *Printed samples with silver contacts*

Figure 4.6: *Printed samples with and without silver contacts. The silver contacts in (b) were printed after the samples in (a) were completely dry.*

mesh, fixed onto a rectangular aluminium frame of dimensions $70 \times 80\ cm^2$ was used as a printing screen. This screen was manufactured by Register Screen (Pty) Ltd, Cape Town, South Africa and had a mesh count of 150 lines per cm. Figure 4.6 (p30) shows printed samples with and without contacts. These printed samples were allowed to dry under ambient room temperatures before any experiments could be performed on them. A list of selected samples and their compositions is shown in table 4.1 below.

Table 4.1: *An account of sample compositions and printed sheets from which random samples were selected.*

Ink	Selected printed sheets				
No.	Particles	USAXS	SALS	SEM	VI
01	mSi	2	1	1	1
02	SiO_2	2	1	1	1
03	Al_2O_3	2	1	1	1
04	TiO_2	2	1	1	1

4.2 Small Angle Light Scattering

In this section, an inhouse-designed and built Small Angle Light Scattering experiment will be presented. One sample was chosen at random from the mSi, SiO_2, TiO_2 and Al_2O_3 PET printed samples and studied using an inhouse-built Small Angle Light Scattering (SALS) experiment. The SALS experiment was designed, built and commissioned inhouse specifically for this purpose. It consisted of a three-axis Huber Rimsting goniometer which was controlled using SMC900 stepper motor controllers, a screen, sample mounting tool, 100 mW Ne-He laser sources and an 18-mega-pixel digital camera connected to a Linux computer for remote image capturing. The SALS experiment was performed on particles in both powder form (i.e. non-printed samples) and in printed layers. The powder samples were on a $75 \times 25 \times 1\ mm^3$ frosted end optical microscope glass slides shown in figure 4.10 on p33.

The SALS experiment consisted of mainly six major steps, which are illustrated using the block diagram in figure 4.7 below. The equipment used included a 100 mW collimated laser source, a sample stage which had to be aligned perpendicularly to the primary beam, a $70 \times 80\ cm^2$ flat screen covered with plain white paper which also had to be aligned perpendicularly to the primary beam, a digital camera which was used to capture the scattering produced on the screen, a computer located in the control room where images could be captured remotely and then processed. The alignment of the source, sample and the screen is illustrated in figure 4.8.

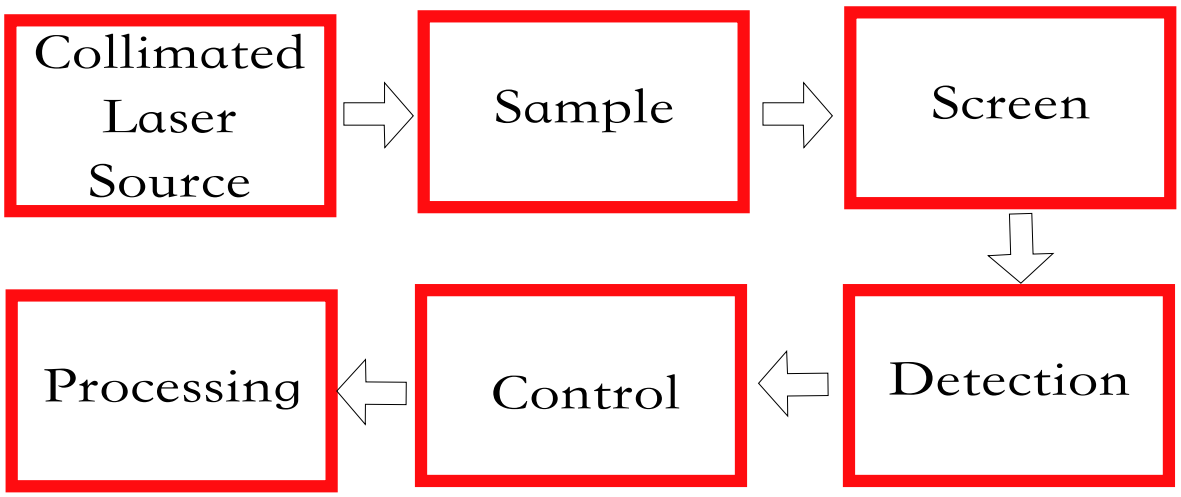

Figure 4.7: *SALS experiment block diagram*

4.2.1 Experimental setup

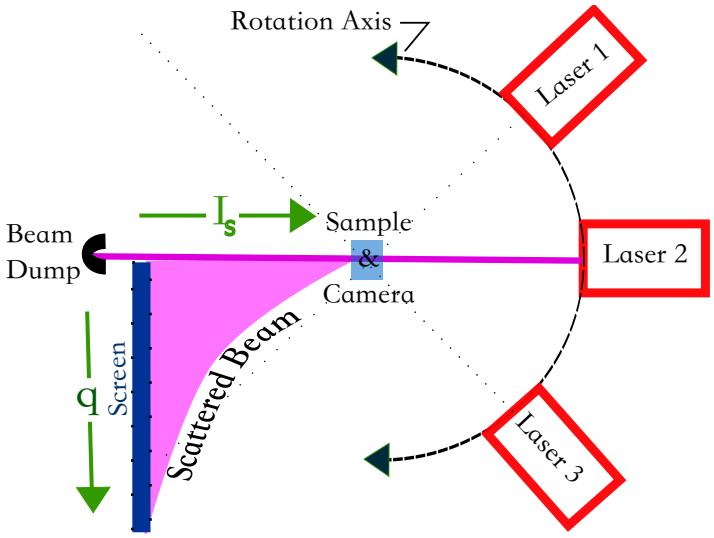

Figure 4.8: *A top-view schema of the SALS experiment setup*

.

HeNe laser sources with different wavelengths (eg. 650 nm, 540 nm and 405 nm) each with a maximum power of 100 mW and an angular spread of $\pm 0.04^o$ were mounted on a vertical arm of the goniometer for accurate horizontal alignment of the laser beam from the different laser sources with the sample and the screen.

An imaging of the scattered light technique was achieved using an 18-mega-pixel web-cam connected to a computer in the control room. Figure 4.8 schematically illustrates the inhouse-setup that was used. No pinhole was included in the setup since it often resulted in diffraction rings when included. The lasers were collimated and focussed to ± 2 mm beam spot size at the screen 122.5 cm away.

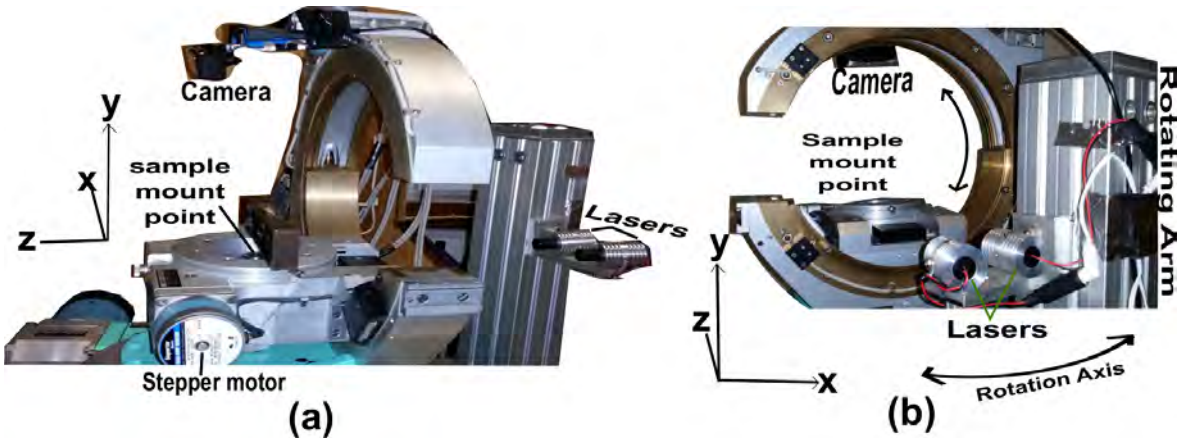

Figure 4.9: *(a) Side view and (b) back view photographs of the SALS setup showing the three rotational axis of the goniometer, two lasers mounted on a rotating arm which is controlled by stepper motors.*

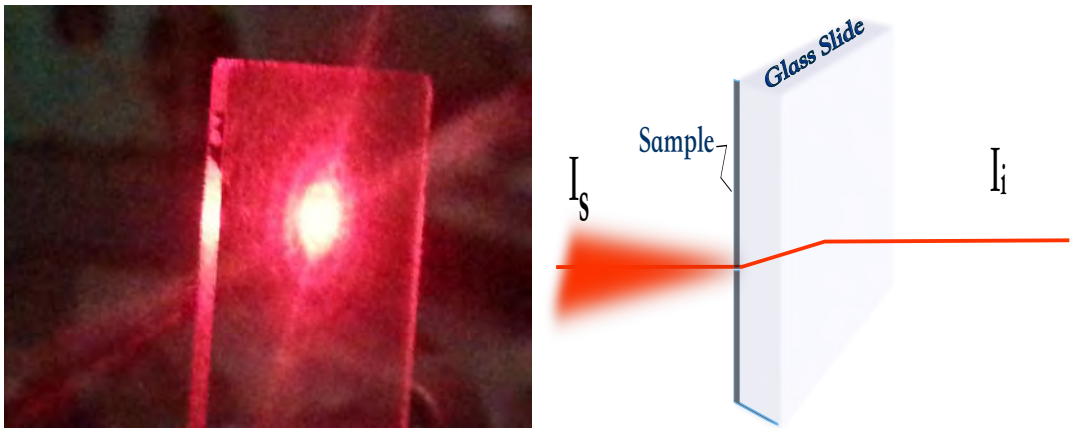

(a) ***(b)***

Figure 4.10: *(a) A photograph and (b) a schema of an illuminated glass slide with powder sample on the beam exit side*

The following steps were followed to align the equipment :-

Step 1: The lasers and the digital camera were mounted on the goniometer as shown in the figure 4.9 (p33). The horizontal axis of the goniometer allowed three lasers to be mounted at the same time. These lasers could be exchanged by just rotating this axis horizontally using stepper motors.

Step 2: The scattering screen was mounted perpendicularly to the beam path. The alignment was achieved by reflecting the primary beam back to the laser source using a mirror mounted flat on a screen surface and ensuring that the backward-reflected beam goes through the exit point of the beam on the laser source. The screen was then secured firmly and the sample to screen distance was recorded.

Step 3: The mirror was removed, allowing the primary beam to pass as closely as possible on one side of the screen and then dumped on a beam-stop behind the screen.

Step 4: The sample was mounted in the beam path, while again maintaining the alignment of the sample holder (i.e. glass slide or PET) with the beam by ensuring that the backward reflected beam again went through the beam exit point on the laser source. This was repeated each time the sample was changed.

Step 5: The sample was replaced by a diffracting grating slide ensuring that the central maxima went straight to the screen dump and the other diffraction points were horizontal on the screen. This was repeated each time the sample or laser sources were changed to monitor the alignment.

Step 6: An 18-mega pixel digital camera was mounted directly above the sample on the goniometer. An image of the screen from this camera was aligned on a computer LED display and then focused appropriately, after which the auto-focusing function of the camera was turned off. The digital camera was then secured firmly.

4.2.2 Calibration setup

The 8-mega pixel digital camera output was connected to a computer in the control room to record images of the screen in the experiment room. A software algorithm based on a free software project that produces libraries and programmes for handling multimedia data known as "ffmpeg" was specifically developed and used to control the webcam to capture the scattering screen image for as many times as it was required. The following *ffmpeg* code

```
ffmpeg -f video4linux2 -i /dev/v4l/by-id/"+webcam+" -vframes 1
img"+‘1+i‘+".bmp" |
```

was looped using a python script and images of the screen were captured for each step in the following sequence:-

Step 1: Room lights were left on and the lasers turned off. This was done to record the screen alignment.

Step 2: A diffraction grating was mounted at the sample position on the beam path and the room lights switched off while the lasers were turned on.

Step 3: A blank sample holder (i.e. glass slide or PET) was mounted at the sample position. 200 images were captured with lasers switched on and room lights switched off.

Step 4: A sample was mounted and thereafter, a further 200 images were captured.

Step 5: The sample was replaced with a diffraction grading slide and step 1 was repeated to verify that the alignments remained the same throughout the experiment.

The above steps were repeated for each time the sample or laser source was changed. All images were captured in an uncompressed (i.e. bmp) format.

a) Wavelengths of primary beams

Although all the wavelengths of the lasers were known from their labels, they were further verified using an 80 lines/mm diffraction grating slide placed at the sample position. For a sample-to-screen distance of 122.5 cm, a laser source labelled 640 nm showed six maximum bands (circled with dotted lines for easy identification in figure

4.11) with an average separation of 6.2 cm between them.

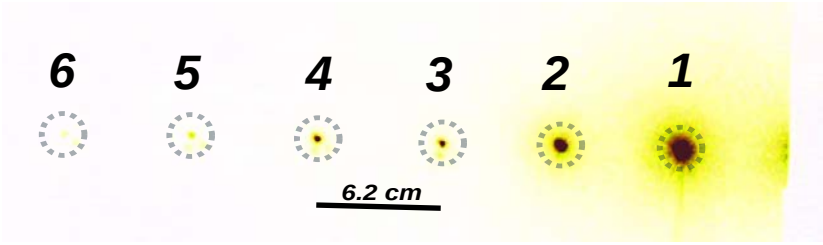

Figure 4.11: *Diffraction spots of an 80 lines per millimetre grating slide placed at 122.5 cm away from the screen*

Each of the diffraction spots corresponded to an order of diffraction n, therefore six diffraction orders (labelled 1 to 6 in figure 4.11) were observed on the screen. The grating element d of the 80 lines/mm grating slide was therefore calculated as:-

$$d = \frac{1}{N} = \frac{1}{80000} = 12.5\mu m, \tag{4.1}$$

with N being the number of grid lines per meter on the grating slide. The angular spread for the first order reflection was obtained as

$$\theta = \tan^{-}\left|\frac{x}{D}\right| = \tan^{-}\left|\frac{6.23}{122.5}\right| = 2.94^{o}, \tag{4.2}$$

therefore

$$\lambda = \frac{\sin\theta}{Nn} = \frac{\sin 2.94^{o}}{80000 \times 1} = 641nm. \tag{4.3}$$

All other wavelengths were verified in the same way.

Since the primary laser beam was made to pass the screen as close as possible to one of its sides, this made its position relative to the screen unknown. However, since the primary beam position on the screen should have been the same as the position of the 0^{th} diffraction order of the grating slide, its position could be obtained from the positions of the corresponding higher orders (harmonics). Therefore the pixel position of the 0^{th} diffraction order was obtained by plotting the pixel positions against their corresponding diffraction orders. An example of such data has been presented in table 4.2.

Table 4.2: *Positions of six diffraction orders of an 80 lines/mm diffraction grating slide placed (at sample position) 122.5 cm from the screen*

n	1	2	3	4	5	6
x	1576	1374	1170	962	744	520

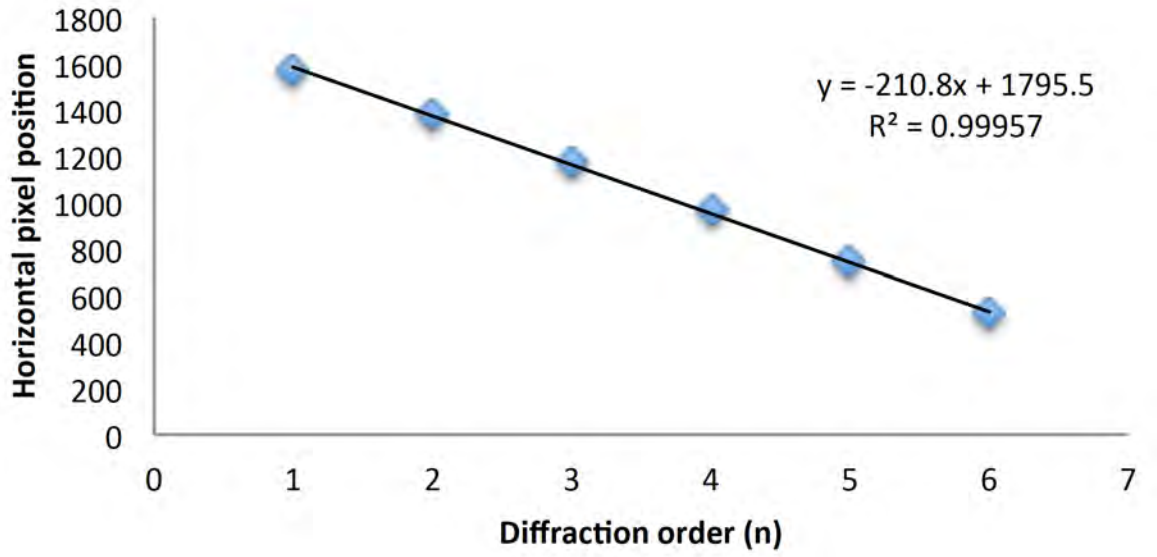

Figure 4.12: *Pixel positions of maximum reflections of the diffraction grating*

The pixel positions in table 4.2 were plotted against corresponding diffraction orders as shown in figure 4.12. The uncertainty values were ±2 pixels hence negligibly small. An intercept of 1795 pixels was obtained and traced back to the pixel position of the 0^{th} order of diffraction as well as to the pixel position where the primary beam would have landed on the screen image.

b) Converting bitmap images to grey scale-values

The bitmap images were converted to grey-scale values using the imageJ program. Two hundred images were stacked together after which they were averaged into one RGB image using the "z-project" feature of the imageJ program. The average image was then converted to a 32 bit bitmap format with same number of pixels as the original image although it contained less data. An ImageMagick "convert" command-line tool from *ImageMagick Studio LLC* was used to convert the bitmap image into a text file containing grey scale values as shown in figure 4.13 [87].

```
0,0: ( 14, 14, 14)  #0E0E0E  srgb(14,14,14)
1,0: ( 12, 12, 12)  #0C0C0C  srgb(12,12,12)
2,0: ( 12, 12, 12)  #0C0C0C  srgb(12,12,12)
3,0: ( 10, 10, 10)  #0A0A0A  grey4
4,0: ( 10, 10, 10)  #0A0A0A  grey4
5,0: (  9,  9,  9)  #090909  srgb(9,9,9)
6,0: ( 10, 10, 10)  #0A0A0A  grey4
7,0: (  9,  9,  9)  #090909  srgb(9,9,9)
8,0: ( 10, 10, 10)  #0A0A0A  grey4
9,0: (  9,  9,  9)  #090909  srgb(9,9,9)
10,0: ( 10, 10, 10)  #0A0A0A  grey4
11,0: ( 10, 10, 10)  #0A0A0A  grey4
12,0: ( 10, 10, 10)  #0A0A0A  grey4
13,0: ( 10, 10, 10)  #0A0A0A  grey4
14,0: ( 10, 10, 10)  #0A0A0A  grey4
15,0: ( 10, 10, 10)  #0A0A0A  grey4
```

Figure 4.13: *Exemplary snippet of the grey scale velues from a bitmap image*

c) Extracting $I(q)$ and q values from the grey scale values

A java algorithm was specifically developed to extract $I(q)$ and q values from the grey scale values using

$$I(q) = (0.299 \times R) + (0.587 \times G) + (0.114 \times B) \tag{4.4}$$

and equation 3.6 on p 15 [88]. The q values were obtained in inverse angstroms (Å^{-1}) whereas the $I(q)$ values were in arbitrary units. The images were scaled before establishing relative distances between pixels. In this way, the data could be represented as scattering curves in log-log scale.

4.2.3 Repeatability and Reproducibility

Since the SALS experiment was an inhouse-designed experiment, it was repeated a number of times to ensure its reproducibility. The experiment was repeated on the same samples many times to ascertain consistency of results. In addition, 200 scattering images were averaged each time before extracting $I(q)$ and q values. Figure 4.14 shows the scattering curves of the same sample during two different measurements under same experimental conditions.

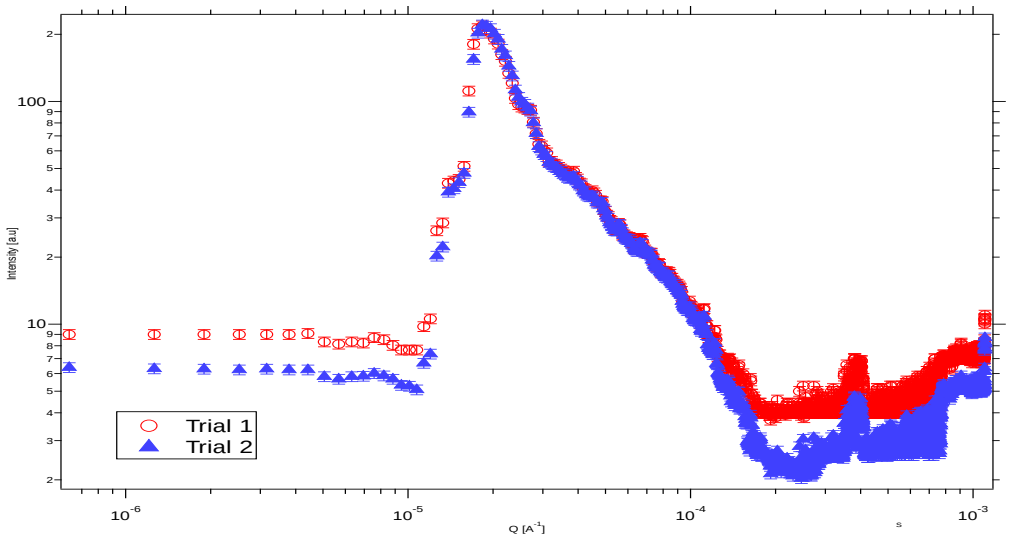

Figure 4.14: *Two SALS data of the same mSi sample in two separate similar experiments using the 405 nm laser*

The two curves in figure 4.14 are identical to within 0.5% difference. The differences are mainly in the background scattering, which is shown in the higher q-range. Similarly the almost flat region on the curve towards the lower q-range indicates the upper limit of the technique where measurements can not be trusted. These regions below $\pm 10^{-5}$ and above $\pm 10^{-4}$ will be ignored during the fitting (e.g. see example of the cropped data in figure 5.1)

The

4.3 Ultra Small Angle X-Ray Scattering

Two sets of printed sheets, one printed on PET and the other on paper, were sent to the Advanced Photon Source Sector 15ID where they were studied using the Ultra Small Angle X-ray Scattering (USAXS). A schematic of setup is shown in figure 4.15 [89] . A standard USAXS instrument and procedure was followed as outlined in literature [5, 93]. This beam had an energy of 16.85 keV and covered a q-range of $1.5 \times 10^{-4}\text{Å}^{-1} < |q| < 1\text{Å}^{-1}$.

The scattered beam from the sample contained both the SAXS and USAXS patterns. Therefore, a second channel cut crystal, which was also made from crystalline silicon (220) was placed after the sample in a rotating axis, which by accurately rotating this second collimating crystal step-wise, the USAXS data could be isolated.

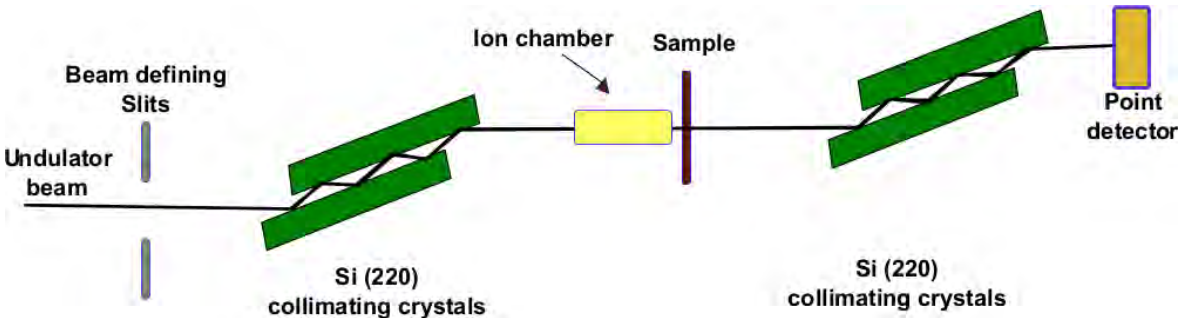

Figure 4.15: *A schematic illustration of the Ultra Small Angle X-ray Scattering experimental setup in one-dimensional collimation configuration [1]*

.

4.3.1 Sample mounting

The samples were cut from the printed sheet and mounted, using a standard (Scotch, Kapton) tape on a sample holder plate shown in figure 4.16 (p 41). Stepper motors were programmatically used to position the samples in-line with the beam. These stepper motors had a precision of $\pm 10\mu m$. Twenty-nine samples and one blank substrate could be mounted at the same time.

4.3.2 Data acquisition

A scintillation type photon-counting detector with good signal to noise ratio was used to collect the USAXS data. This detector was connected to the NIM type electronics

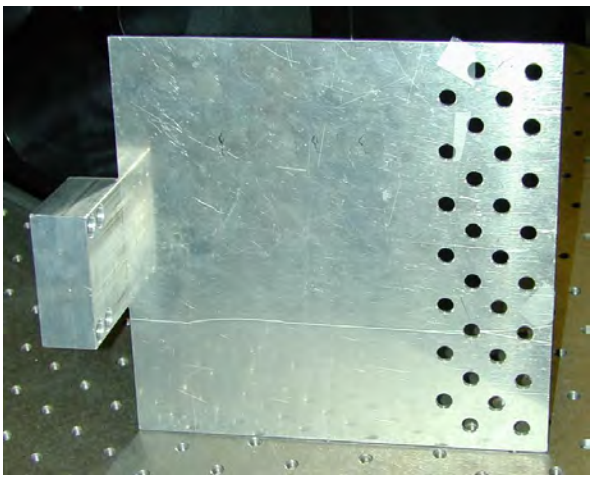

Figure 4.16: *USAXS experiment sample holder showing sample mount points (i.e. holes) [9].*

setup, which allowed separate detector electronics features in separate modules. The data was then saved as electronic files and processed using the Irena package of the IGOR Pro software [89].

4.4 Scanning Electron Microscopy

The third set of printed sheets, which were printed on paper were examined using the Scanning Electron Microscopy (SEM). The SEM experiment was done using a Nova Nano SEM 230. The beam energy was set to 5 keV, Horizontal Field Width (HFW) to 11.9 μm, spot size to 2.0 and a current of 200 pA. An Everhart-Thornley Detector(ETD) was used for secondary electron imaging.

4.4.1 Sample mounting

The printed layers were cut to size and mounted on aluminium stubs. These samples were all earthed to the aluminium stubs using silver impregnated paint and thereafter carbon coated using an evaporation coater to reduce charging. This enhanced the image quality at higher magnifications.

4.4.2 Data acquisition

The 80000×, 50000×, 25000× and 10000× magnifications were used. After the necessary focusing and alignment was achieved, a random spot was chosen and images were taken using these magnifications from highest to smallest. In cases where the samples

were statically charging, as in the case of Al_2O_3 the sample was carbon coated again before further measurements were taken. The SEM results will be presented in section 5.2 on p56.

4.5 Electrical characterisation

The last set of printed sheets that were on paper were taken through the diode current-voltage (IV) measurements. The voltage-current (VI) measurements of the samples in table 4.1 (p31) were measured using a Keithley 4200 semiconductor characterisation system. This system can handle current between 0.1 fA and 1 A as well as voltage between 1 μV and 210 V in real-time.

4.5.1 Sample mounting

All samples studied in this section were printed layers on paper substrate. The samples were dried using a pre-heated oven at 100^oC for 60 s. The Keithley 4200 semiconductor characterisation system is commonly used for electrical characterisation of electronic devices(e.g. transistors). It has an embedded computer running a Windows XP operating system. It also has an application software for performing real time current-voltage sweeps. There are two Source Measurement Units (SMUs) on a Keithley 4200 which can source current and voltage with a supply-measurement range and a sample holder with two spring loaded probes were connected on two of the three sample terminals at a time as shown in figure 4.17 (b).

4.5.2 Data acquisition

Current was swept between -1 nA and 0.1 nA in steps of 0.2 nA with a sweep delay of 0.2 s and hold time of 1 s , while measuring the corresponding voltage. This resulted in 101 V and I measurement points. The Keithley 4200 also allowed *in-situ* measurements of resistance (R) values. The Voltage-Current(VI) measuring equipment is shown in figure 4.17.

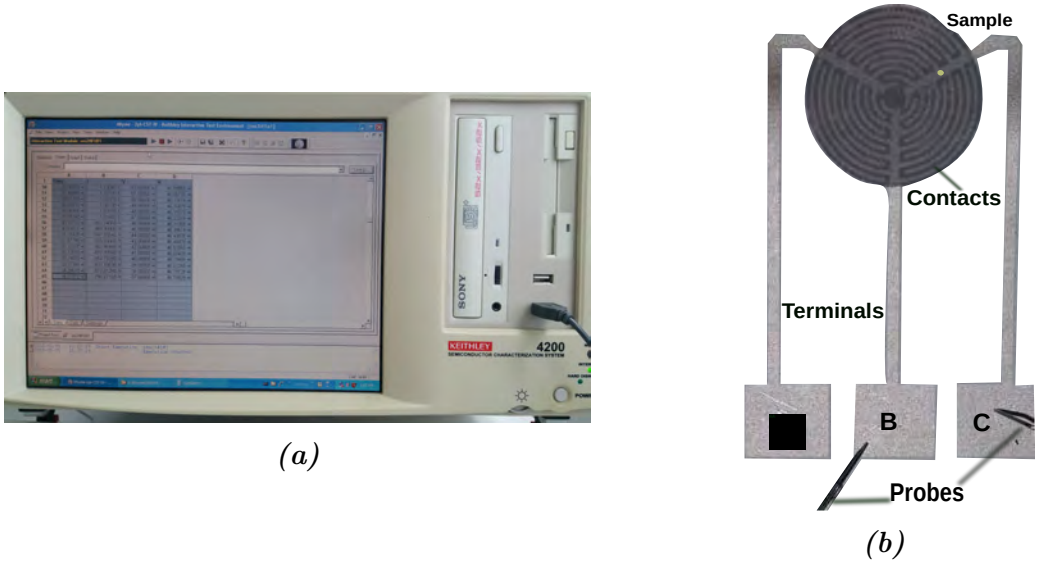

Figure 4.17: *Voltage-Current(VI) measuring equipment where (a) is a front panel of a Keithley 4200 semiconductor characterisation system and (b) is a sample with silver contacts and probes on the second(B) and third(C) contact points.*

Chapter 5 Results

In this chapter, the experimental data for the structural and electrical characterisation of the studied materials will be presented and later discussed in chapter 6. The data for the structural characterisation includes the small angle scattering and spectroscopy. The SAS data, which consists of SALS and USAXS will be presented mainly in the form of log-log scale graphs of $I(q)$ vs q. The unified-power law equation will then be used to fit the SAS data and to extract physical parameters such as the radius of gyration (R_g) in section 5.1. SEM micrographs will also be presented alongside the SAS data. The electrical characterisation data will be presented as graphs of voltage against current (i.e. VI curves) and later analysed using modelled particle-to-particle connections in section 5.3.

5.1 Small Angle Scattering

5.1.1 SALS

a) Blank sample holders

Three different glass slides were used each time (i.e. one as a blank and the others holding mSi and SiO_2 samples). The scattering data of the same three slides were compared to check if they scattered light differently under same experimental conditions and the results are plotted in figure 5.1. Each plot was again obtained from an average of 200 scattering images. The pixel intensities far away from the primary beam were completely dark, same as when no lasers were turned on. This suggested that camera had a uniform(flat) response and showed no dark current signal.

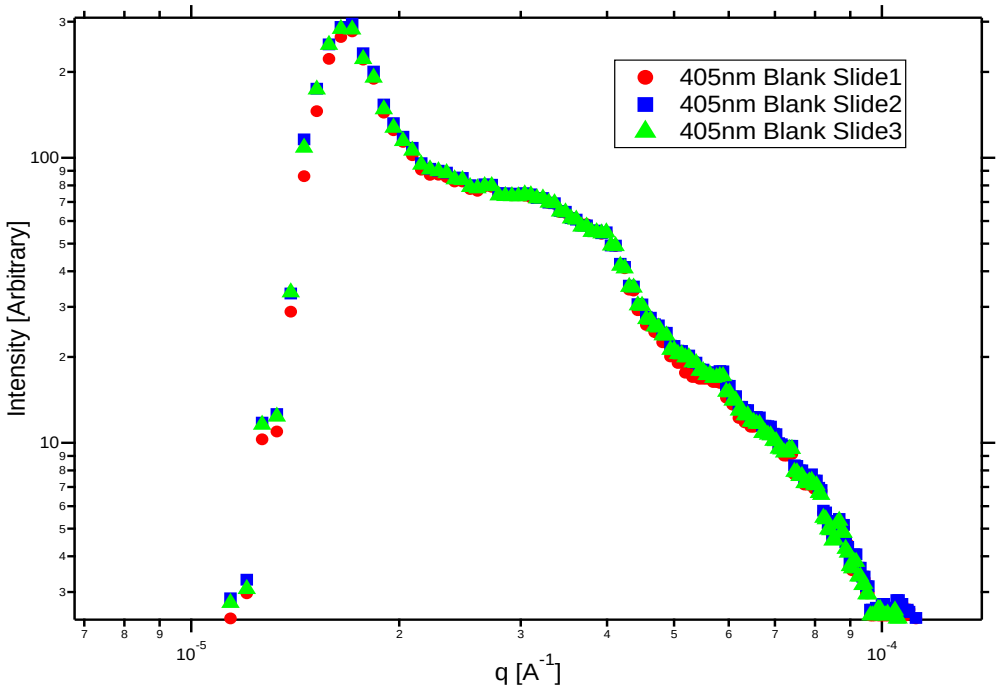

Figure 5.1: *SALS data of three clean slides using a 405 nm laser*

The results presented in figure 5.1 indicate that the scattering curves of the three clean slides were identical, which implied that these three slides could be used interchangeably during measurements.

b) SALS Data

After subtracting the scattering effects of the blanks from the scattering data, the following SALS data was obtained and presented in figure 5.2 for (a) mSi, (b) SiO_2, (c) Al_2O_3 and (d) TiO_2. The mSi and SiO_2 SALS data generally show what appears to be a single Porod region, after which the data flattens off at lower q-ranges as the upper experiment limit of the setup is reached. The Al_2O_3 and TiO_2 show clear Guinier "knees" shapes separating size ranges.

This SALS results constitute a very narrow q-range (i.e. only one order of magnitude) and will therefore be combined with the USAXS data in section 5.1.3. The extreme ends of the SAS data (i.e extreme upper and lower q-ranges) generally contains experimental artefacts and will therefore be cropped out.

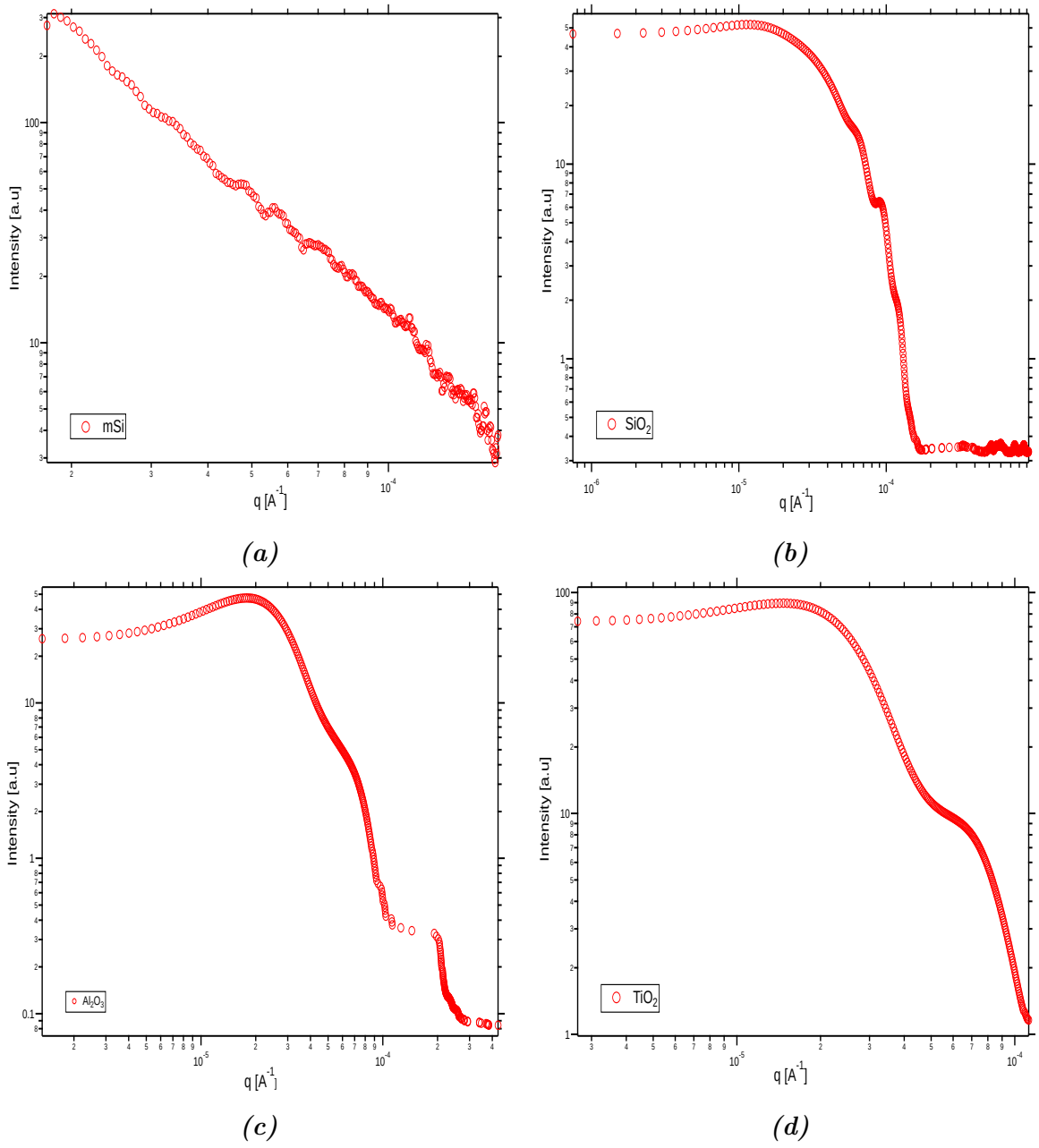

Figure 5.2: *SALS results of (a) mSi, (b) SiO_2, (c) Al_2O_3 and (d) TiO_2 samples*

5.1.2 USAXS

Figure 5.3 shows background corrected and desmeared USAXS scattering curves of (a) mSi, (b) SiO_2, (c) TiO_2 and (d) Al_2O_3 respectively.

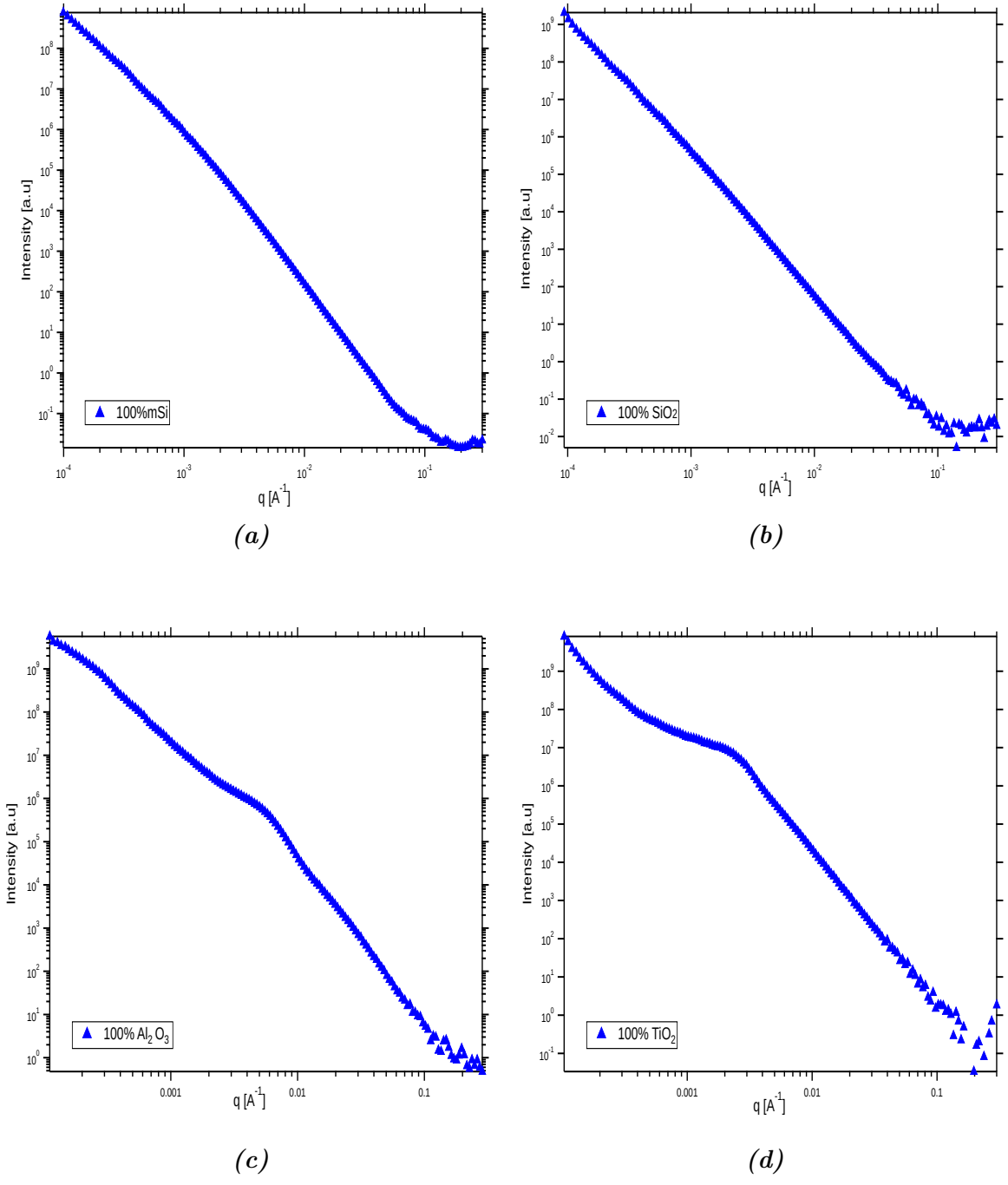

Figure 5.3: *USAXS curves of pure materials (a) mSi, (b) SiO_2, (c)Al_2O_3 and (d) TiO_2*

The mSi and SiO_2 data appears to consist of a single broad Guinier knee with only one reasonable level to fit, whereas the Al_2O_3 and TiO_2 exhibit sharp Guinier knees, one for TiO_2 and two for Al_2O_3. The second Guinier knee of the Al_2O_3 data is not clearly pronounced towards the upper region of the curve (low q range).

5.1.3 SALS and USAXS combination

Different laser sources with different wavelengths (i.e. 640 nm, 532 nm and 405 nm) were used. However, the resulting scattering data from these different wavelengths overlapped with each other when used under the same conditions. Figure 5.4 shows an example of such an overlap with mSi powder sample. The SALS results from using the three wavelengths are combined with the USAXS data thereby extending the lower q-range of the USAXS data closer to the primary beam.

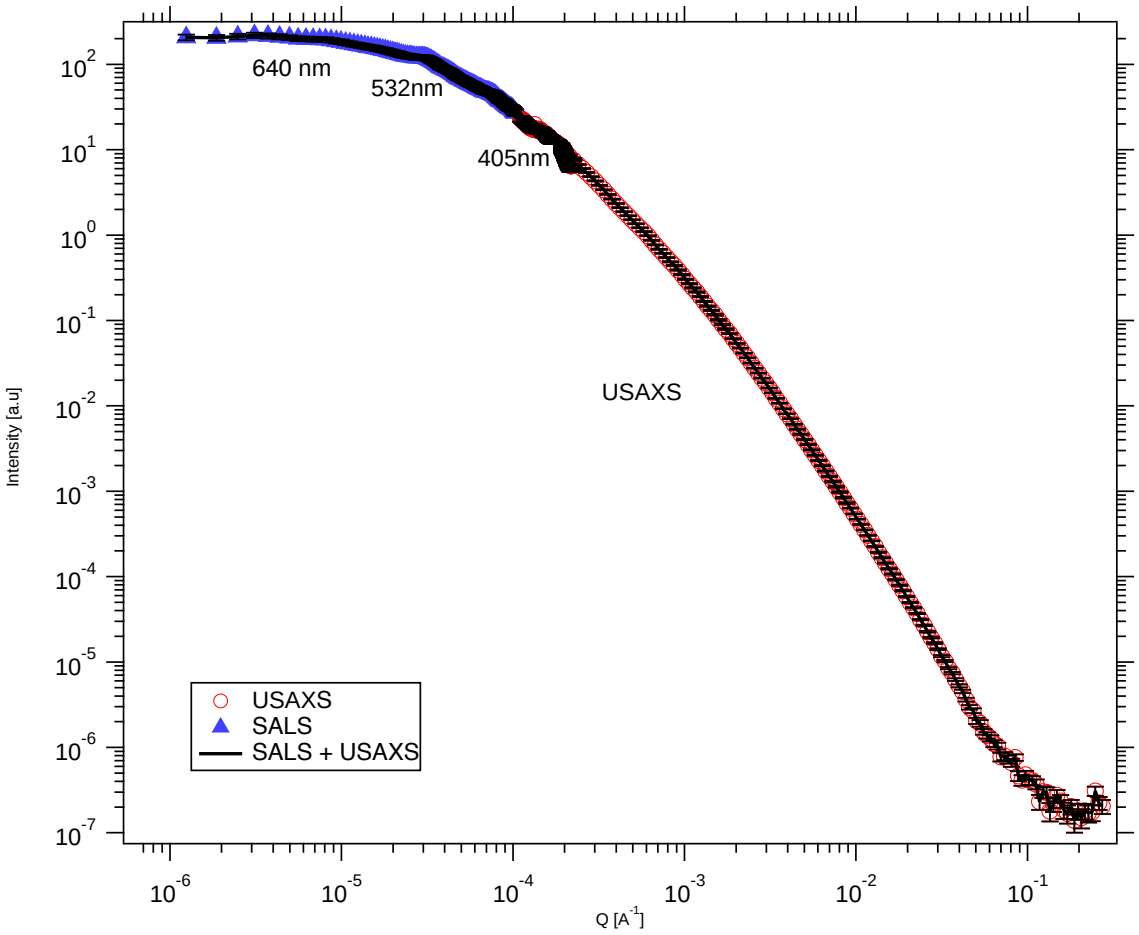

Figure 5.4: $\log I(q)$ *vs.* $\log q$ *plots of mSi SALS and USAXS data.*

All experiments were performed on printed layers except for SALS on mSi and SiO_2, which were performed on powder samples because their printed layers were impenetrable enough to record scattering data on a far screen.

The 640 nm, 532 nm and 405 nm SALS data overlapped remarkably with each other and thereby necessitating only one wavelength to be used. The 405 nm wavelength laser was therefore used throughout all SALS measurements.

Figure 5.5 demonstrates a process used to combine the SALS and USAXS data. In figure 5.5 (a) and (b), SALS and USAXS data are respectively presented separately. In figure 5.5 (c) the SALS and USAXS data are then plotted on the same set of axes after which the SALS data is finally shifted vertically upwards on the intensity axis to align with the USAXS data in figure 5.5 (d).

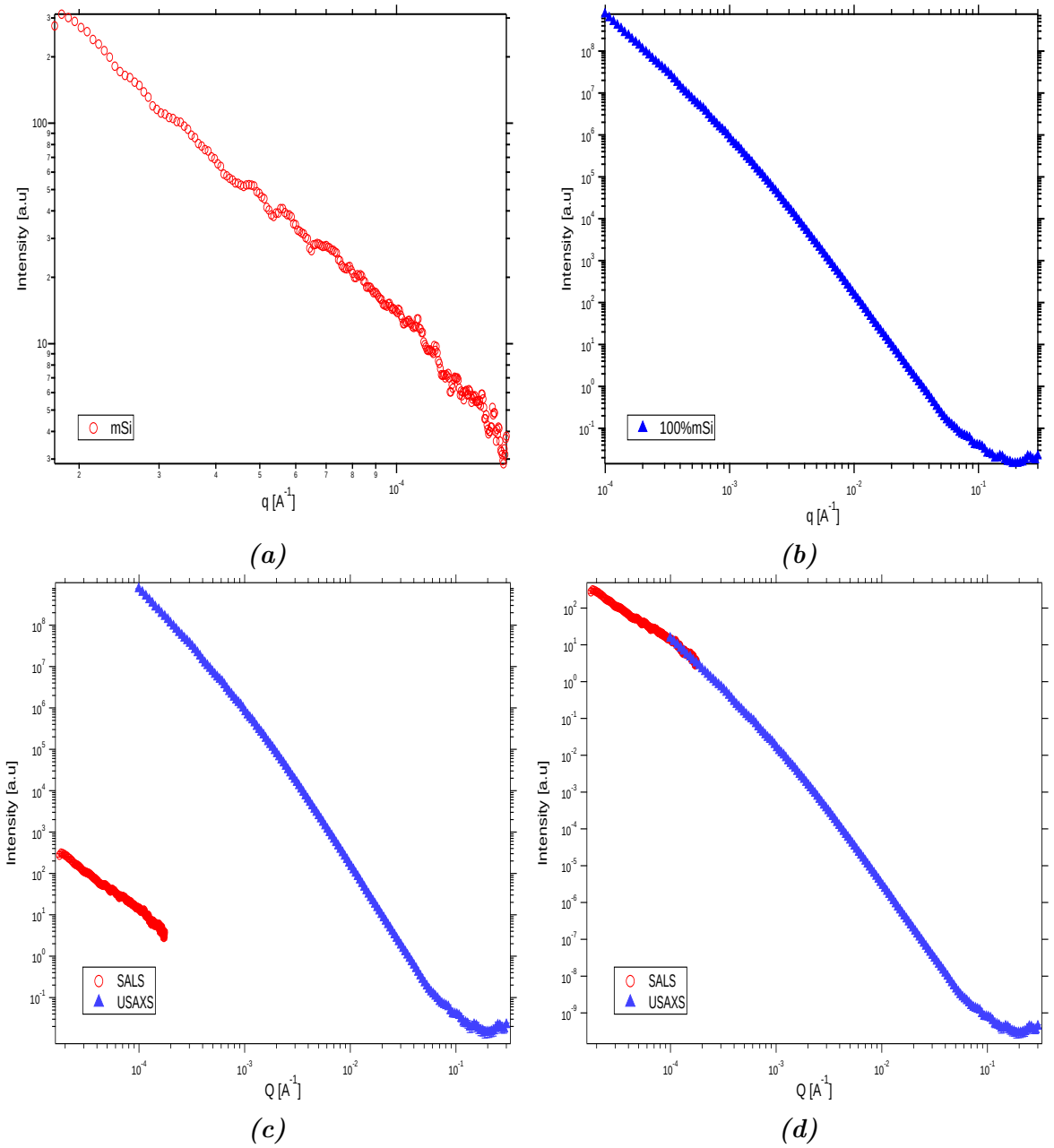

Figure 5.5: *Combined SALS and USAXS data of mSi, where(a) is the SALS data , (b) is the USAXS data, (c) is the USAXS and SALS data before aligning the intensities in (d)*

The SALS data appears to be extending the upper straight region of the USAXS data after which it flattens off towards the lower q-region.

Similarly, figure 5.6 demonstrates a process used to combine the SiO_2 SALS and USAXS data. The curves are presented as (a) SALS and (b) USAXS, (c) the SALS and USAXS data on the same set of axes after which they are aligned vertically in figure 5.6 (d).

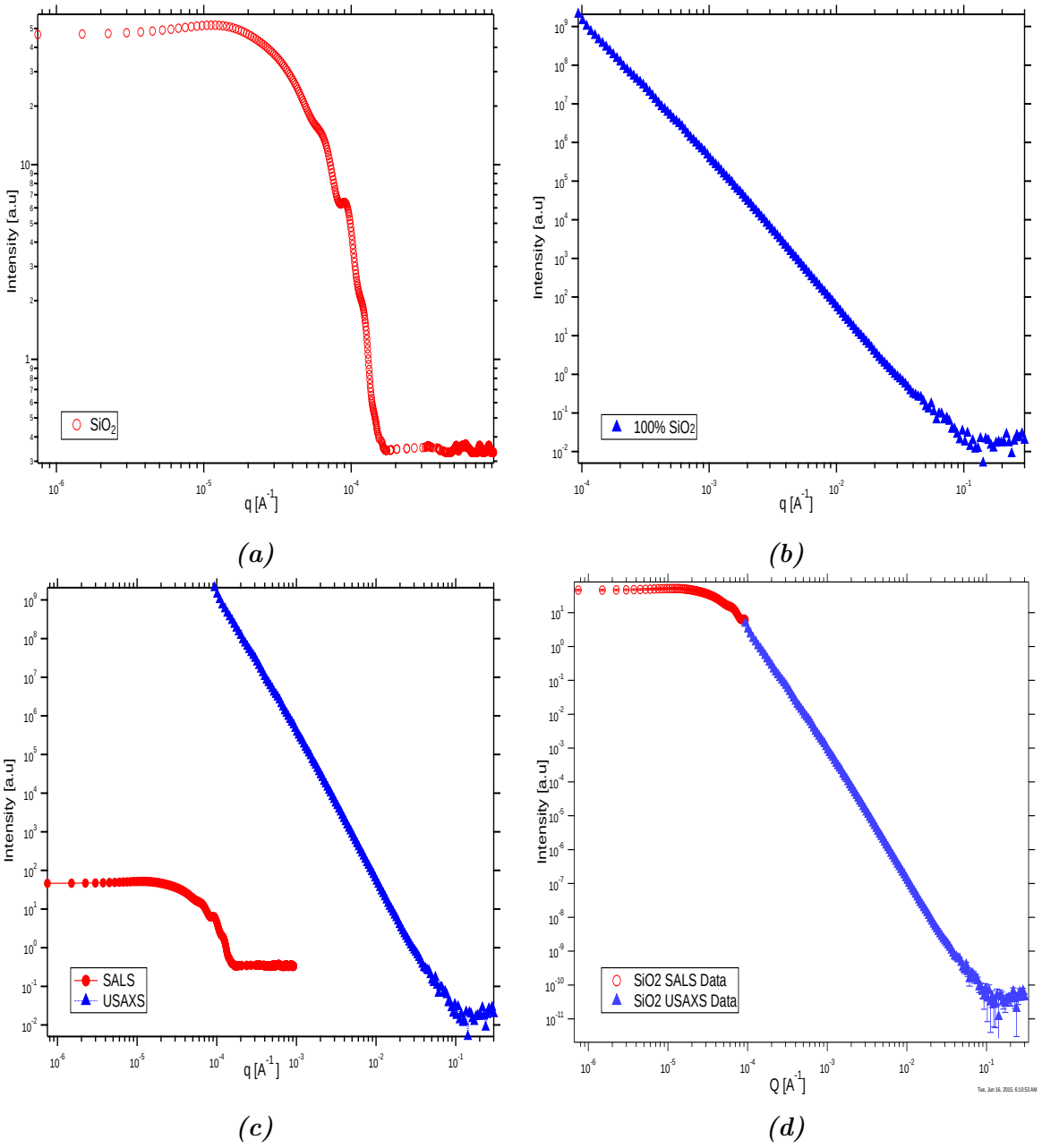

Figure 5.6: *Combined SALS and USAXS data of SiO_2, where(a) is the SALS data , (b) is the USAXS data, (c) is the USAXS and SALS data before alighning the intensities in (d)*

The SiO_2 SALS data in figure 5.6 seems to mainly pronouncing the upper Guinier knee towards the top flat part of the curve.

In figure 5.7 (a) and (b), Al_2O_3 SALS and USAXS data is presented separately. In figure 5.7 (c) the SALS and USAXS data are then plotted on the same set of axes after which they are aligned vertically in figure 5.7 (d).

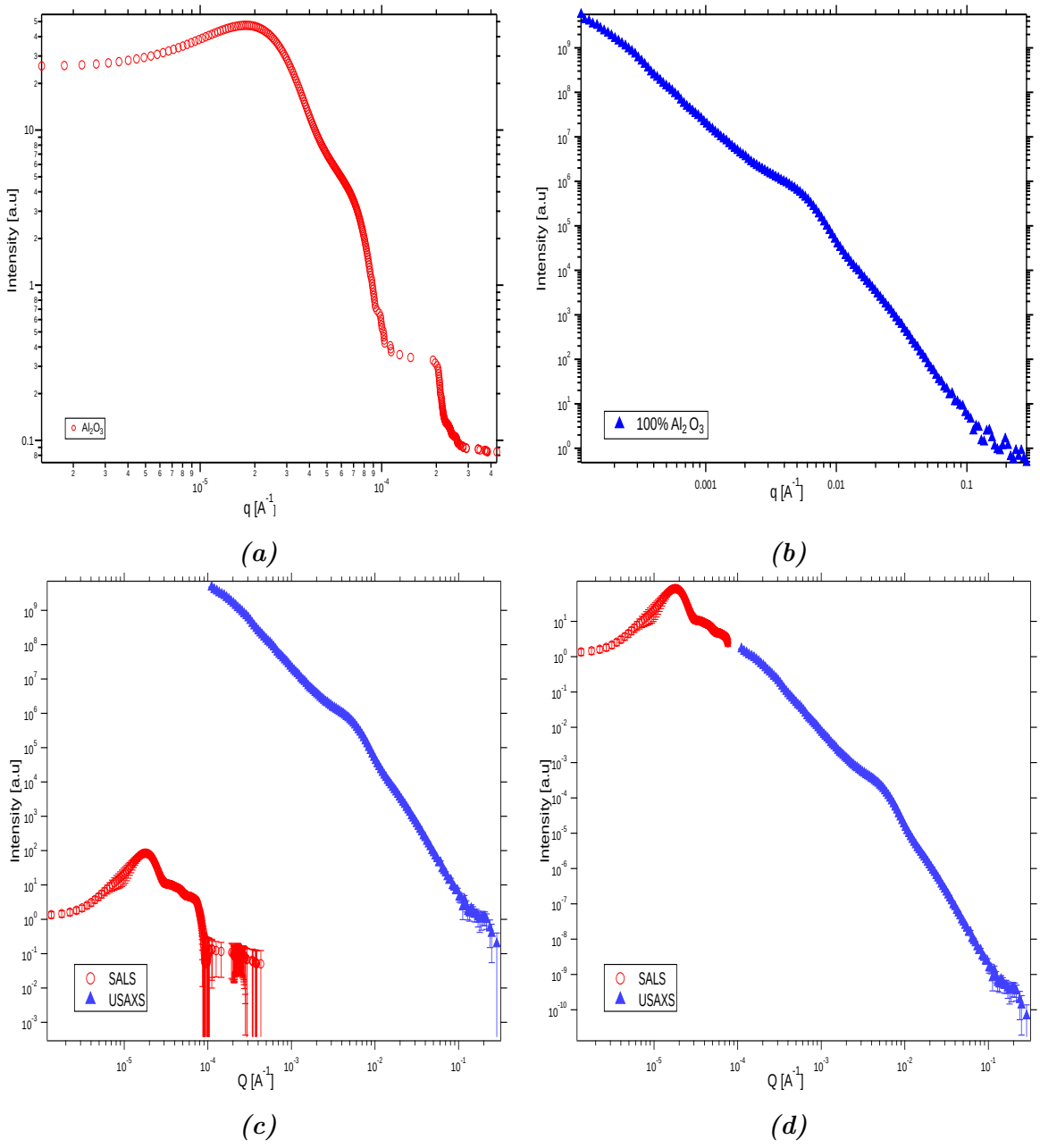

Figure 5.7: *Combined SALS and USAXS data of Al_2O_3, where(a) is the SALS data, (b) is the USAXS data, (c) is the USAXS and SALS data before aigning the intensities in (d)*

A small gap appeared between the SALS and USAXS due the large uncertainties in the SALS background data (figure 5.8c), which were cut off before the two curves were aligned. The Guinier knees on the SALS data looks like peaks on the combined SALS and USAXS data due to re-scaling of the intensity, hence no evidence of correlation.

Similarly, figure 5.8 shows TiO_2 (a) SALS and (b) USAXS data separately. In figure 5.8 (c) the SALS and USAXS data are then plotted on the same set of axes after which they are aligned vertically in figure 5.8 (d).

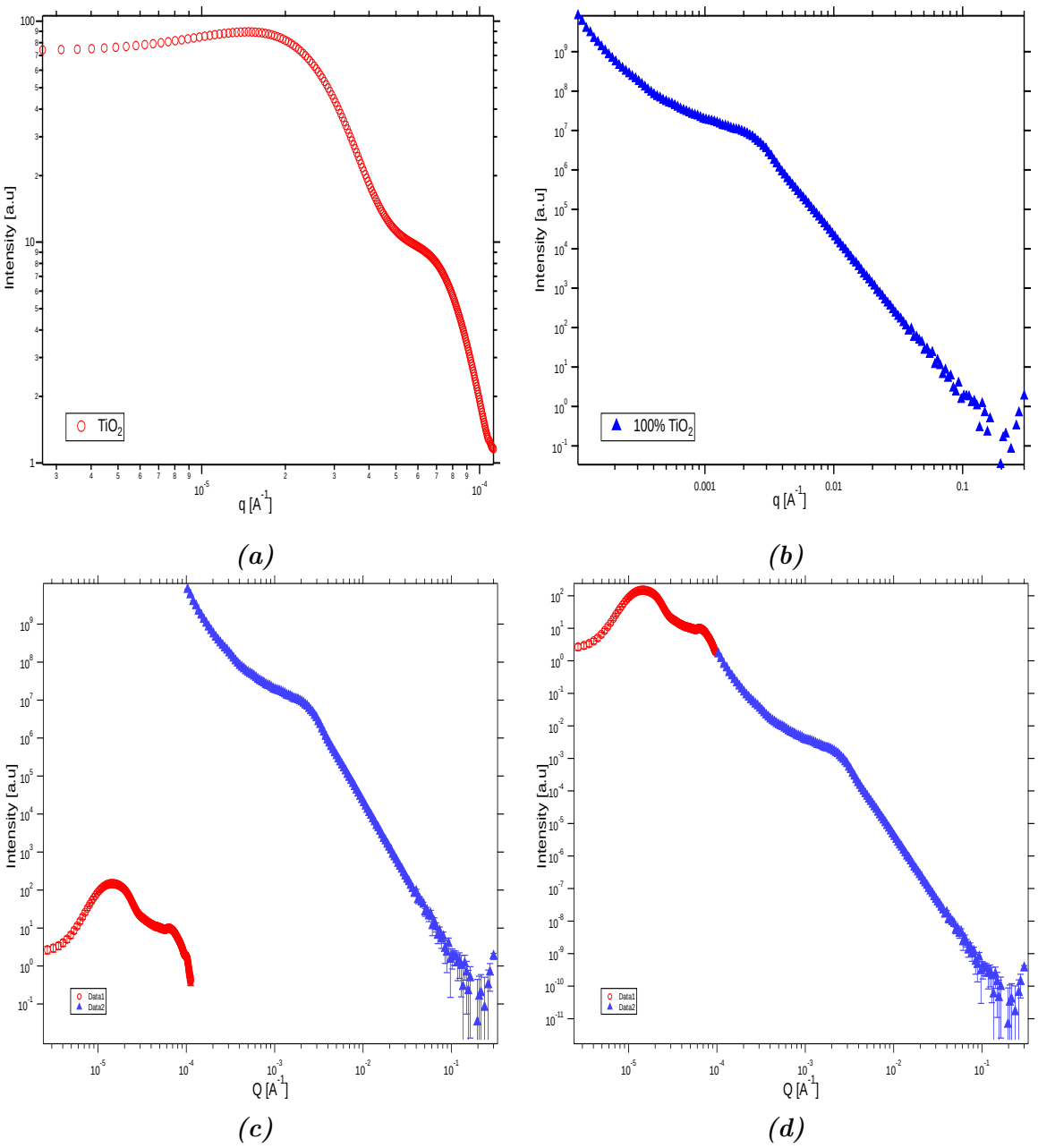

Figure 5.8: *Combined SALS and USAXS data of TiO_2, where(a) is the SALS data, (b) is the USAXS data, (c) is the USAXS and SALS data before aigning the intensities in (d)*

The TiO_2 SALS data seems to be introducing another level, presented by an extension of the last Porod region of the USAXS data in the lower q-range and two Porod regions.

5.1.4 Unified fitting

a) Unified fitting - USAXS

Even before the SALS data was combined with the USAXS data, the USAXS data was fitted using the unified calculated intensity as shown in figure 5.9. It is worth noting the limits of this data towards the lower q so as to appreciate the extension of this region with an addition of the SALS data.

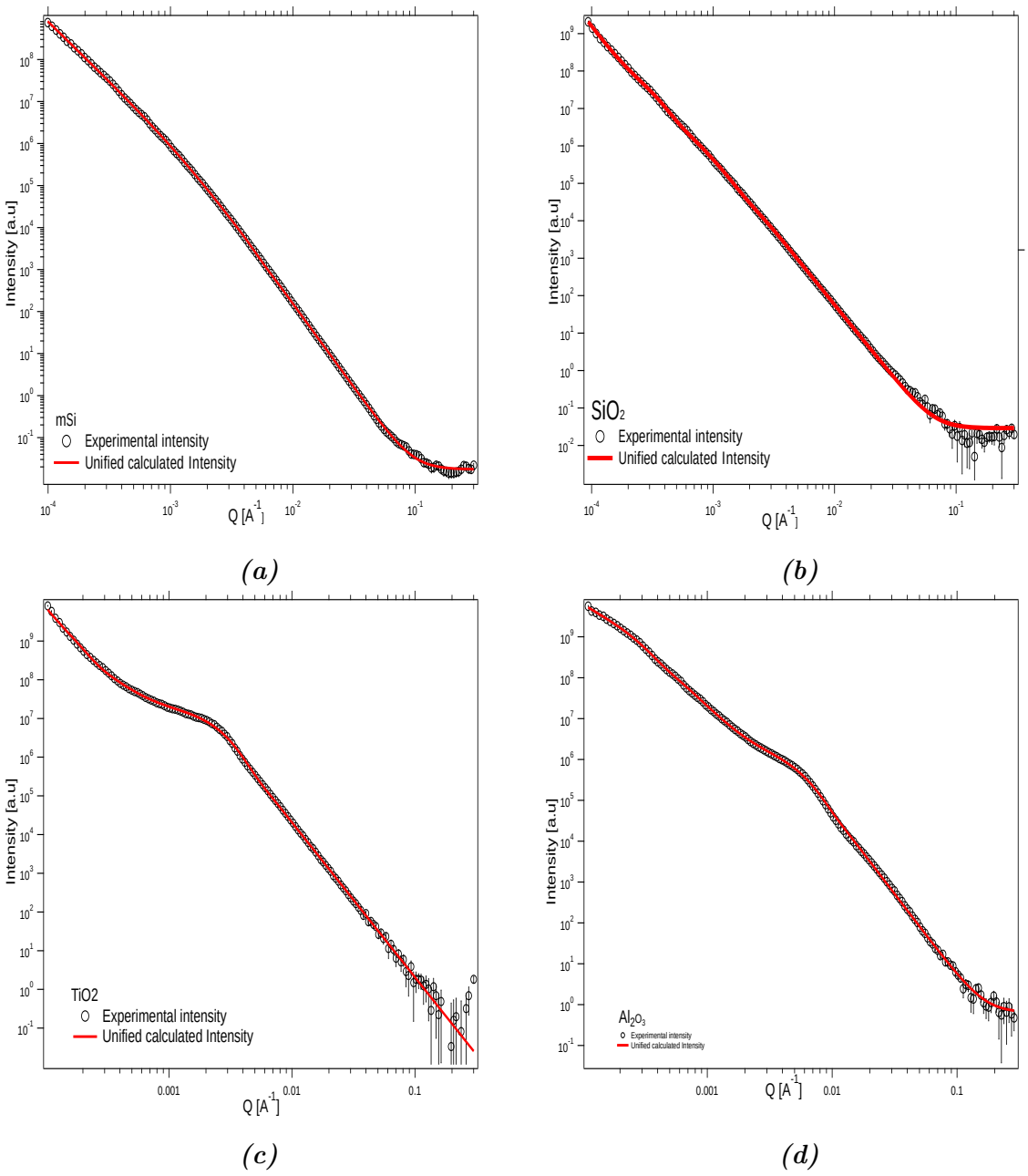

Figure 5.9: *Unified fitting of the (a) mSi, (b) SiO_2, (c) TiO_2 and (d) Al_2O_3 USAXS data*

b) Unified fitting - SALS &USAXS

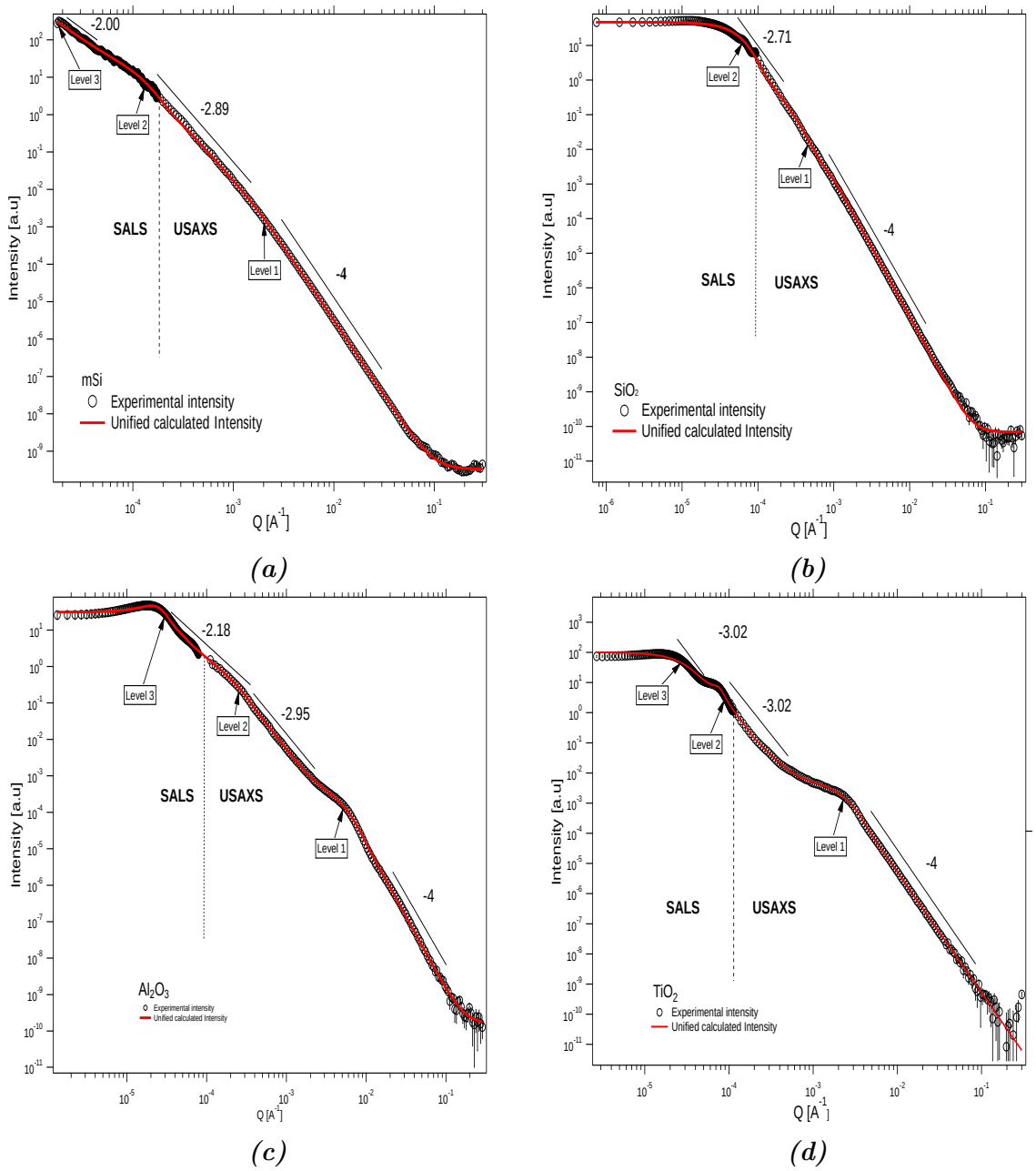

Figure 5.10: *Unified fitting of the (a) mSi, (b) SiO_2, (c) TiO_2 and (d) Al_2O_3 SALS and USAXS data combination. The solid line represents the unified fit to the data. The power law regions for all structural levels and the Porod slopes are indicated on the plot as well as the SALS and USAXS regions*

All samples, whether printed layers or powder samples, generally displayed Porod scattering at high q for the primary particle structural level. In the case of mSi and SiO_2, only one level could be fitted on the USAXS data whereas after combining USAXS with SALS data, at least one extra level could be fitted to provide valuable information about their clusters. Tables 5.1 and 5.2 shows the SAS Unified-fitted data and the calculated scaling parameters for aggregates respectively.

Table 5.1: *SAS Unified-fitted data of the combined SALS and USAXS techniques.*

Unified Fitting							
	Data	**Level**	**G**	R_g [Å]	**B**	**P**	**S/V** $[m^2/cm^3]$
mSi	USAXS SALS	L1 L2	3.03e-03 ±4e-5 20.4±0.960	973±3.00 15000±241	3.19e-14±1.46e-16 5.95e-11 ±3.08e-13	4 .00 2.85 ±6e-04	57.8
SiO_2	USAXS SALS	L1 L2	6.09e-03 ±1.136e-04 46.9±0.417	2738±101 30500±77.1	1.55e-15±6.35e-18 4.08e-12 ± 2.756e-14	4.00 2.9506±7.47e-04	24.9
Al_2O_3	USAXS USAXS SALS	L1 L2 L3	4.57e-04 ±1.01e-05 0.607 ±0.0145 80.7±4.87	371.54±2.95 7460±476 65600±2290	1.38e-13 ±7.81e-16 7.62e-12±1.10e-12 2.80e-09 ±3.81e-09	4.00 2.95±1.89e-02 2.18±0.136	118
TiO_2	USAXS SALS SALS	L1 L2 L3	5.15-03±4.03e-05 7.49 ±1.41 803±65.2	821±3.40 22000± 932 70800± 59742	5.18e-14 9.48e-13 1.18e-12 ±2.32e-13	4.00 3.02 3.03	46.8

Table 5.2: *Calculated scaling parameters for aggregates [10]*

Calculated scaling parameters	**Magnitudes**			
	mSi	SiO_2	Al_2O_3	TiO_2
Degree of aggregation, z	6758±329	7680.83±65.6	1391±319.2	1456±275
Sauter mean diameter, d_p (nm)	104±4.45	241	50.7	128
Geometric standard deviation, σ_g	0.383	0.425	1.39	0.294
Minimum dimension, d_{min}	2.37±1.57e-01	1.64±0.00287	3.77±70.96	1.85±0.421
Connectivity dimension, c	1.12±7.94e-02	1.80±0.0316	0.783	1.64±0.388
Branch fraction,ϕ_{br}	0.767±6.12e-03	0.981±0.00390	-6.35±-0.423	0.941±0.0690
Polydispersity index(PDI)	5.837 ±0.11	8.77±0.0361	3.561±0.140	2.83±0.058

5.2 Scanning Electron Microscopy

In this section, results of the SEM investigation on the sixteen samples will be presented in a comparative manner. The SEM micrographs are presented in figure 5.11.

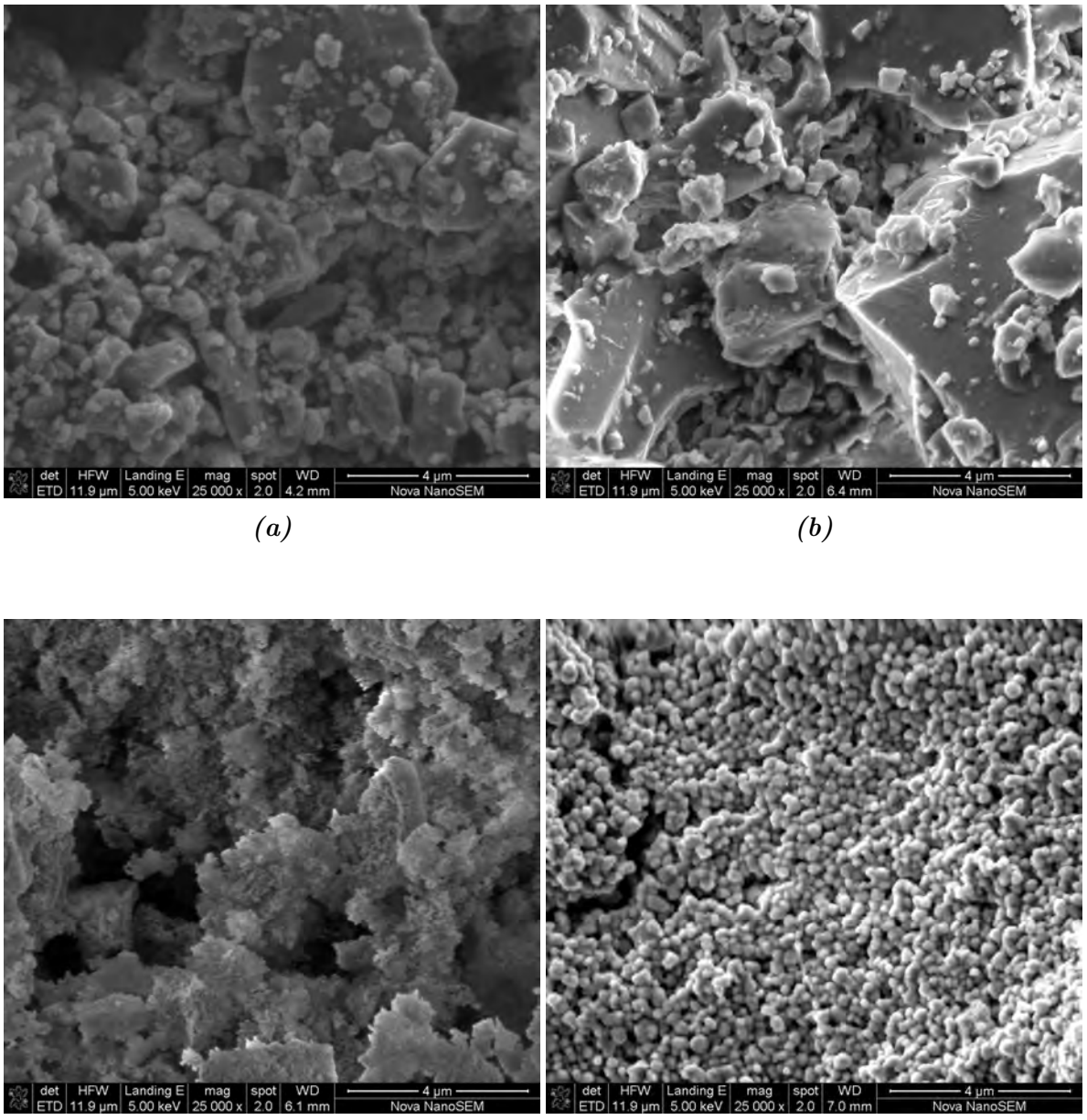

(a) ***(b)***

(c) ***(d)***

Figure 5.11: *SEM images of pure (a) mSi, (b) SiO_2, (c) Al_2O_3 and (d) TiO_2*

The *mSi* SEM micrograph in figure 5.11(a) shows highly poly-disperse sizes and shapes of primary particles. There is evidence of individual particles, which are as big as ± 4 μm like the one close to the top right hand corner of the picture. The *mSi* particles also appear to be compact with smaller particles adhering to the surfaces of bigger ones.

Just like the *mSi* particles, the SiO_2 particles in figure 5.11(b) also reveals highly poly-

disperse sizes and shapes of primary particles. There is evidence of particles, which are over 4 μm big, much like the one close to the bottom right hand corner of the picture. The SiO_2 particles appear to be less compact compared to mSi with smaller particles visible around bigger ones. SiO_2 particles appears to be having sharper edges compared to mSi particles.

Unlike mSi and SiO_2 particles, the Al_2O3 particles in figure 5.11(c) seems to be flaky when on a 25 000 times magnification micrograph. Upon further magnification of the same sample to 80 000 times as later shown in figure 6.3 on p66, the particles also appears to be smudged and fused together. There is however evidence of much smaller particles compared to the mSi and SiO_2 particles.

The TiO_2 particles in figure 5.11(d) seem generally smaller and spherical compared to the mSi, SiO_2 and Al_2O_3. The size distribution of the particles seem to be generally mono-disperse.

5.3 Electrical characterisation

Figure 5.13 shows V against I curves of (a) mSi, (b) SiO_2, (c) TiO_2 and (d) Al_2O_3 samples respectively, where all voltage and current values were each averaged over five samples.

These curves generally looked the same for all samples, since all materials studied in this research were semiconductors. The surface properties of the particles were expected to be different from their material bulk properties due to the presence of the binding material amongst other things. Therefore, the capacitive and diode behaviour shown in figure 5.13 parabolic form was thought to be originating from the particle interfaces as schematically illustrated in figure 5.14 (a) and (b) respectively. The bulk of these particles had parasitic resistances as schematically illustrated in figure 5.14 (a) and (b).

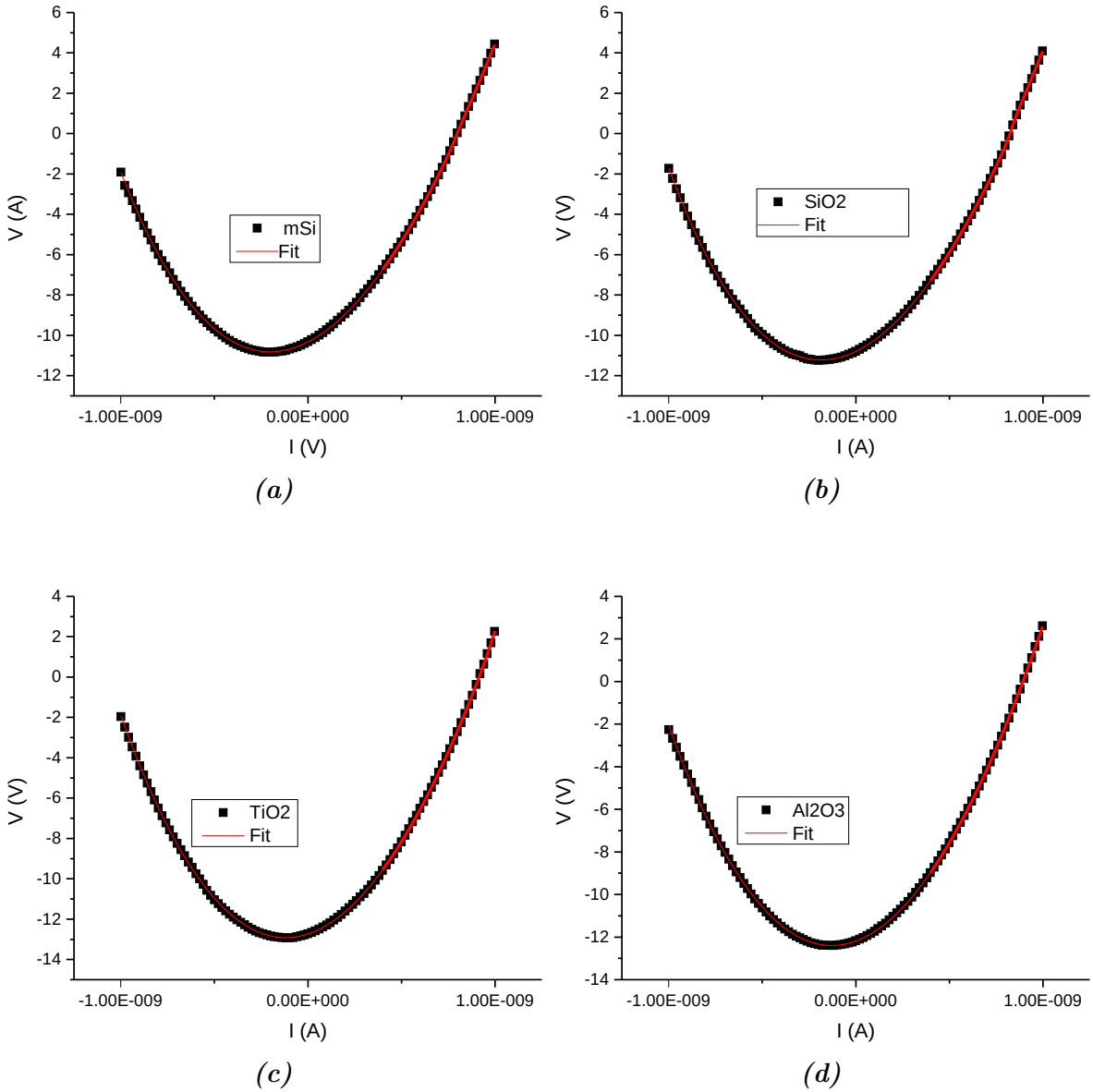

Figure 5.13: *VI characteristics of selected samples*

Therefore, an equivalent circuit of the electrical properties of the printed layers was derived from the model shown in figure 5.14, with two diodes connected back-to-back and the overall capacitance connected in parallel.

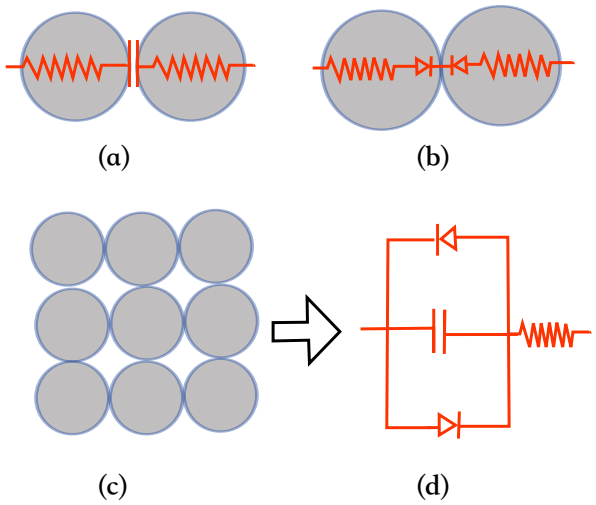

Figure 5.14: *A model of the electrical properties of two semiconducting particles in contact*

The current across a diode is generally given by,

$$I_D = I_s \left[\exp\left(\frac{V_D}{\eta V_T}\right) - 1 \right], \tag{5.1}$$

where I_s is the saturation current, $V_T = kT/e^-$ is the parasitic thermal voltage and η is the ideality factor specific to the type of diode [91]. The parasitic resistance can therefore be included in equation 5.1 as follows:-

$$I_D = I_s \left\{ \exp\left[\frac{V_D - V_{ps}}{\eta V_T}\right] - 1 \right\} = I_s \left\{ \exp\left[\frac{e^-(V_D - IR_{ps})}{\eta k_B T}\right] - 1 \right\}, \tag{5.2}$$

where I_{ps} is the current lost due to the parasitic resistance.

Therefore, the individual currents in the two diodes in figure 5.14 (d) can be represented as

$$I_1 = I_s \left\{ \exp\left[\frac{e^-(V_D - IR_{ps})}{\eta k_B T}\right] - 1 \right\} \tag{5.3}$$

and

$$I_2 = -I_s \left\{ \exp\left[\frac{-e^-(V_D - IR_{ps})}{\eta k_B T}\right] - 1 \right\} \tag{5.4}$$

respectively, which can then be added together to give the overall current according to

$$I = I_{1+2} = I_s \left\{ \exp\left[\frac{e^-(V_D - IR_{ps})}{\eta k_B T}\right] - 1 \right\} - I_s \left\{ \exp\left[\frac{-e^-(V_D - IR_{ps})}{\eta k_B T}\right] - 1 \right\} \quad (5.5)$$

assuming that the materials are symmetrical (i.e. I_s and η to constant). Equation 5.5 can be rearranged to give V_D as

$$V_D = \frac{\eta k_B T}{e^-} \ln \left| \frac{1}{2} \left\{ \left(\frac{I}{I_s} + \Delta I\right) + \sqrt{\left(\frac{I}{I_s} + \Delta I\right)^2 + 4} \right\} \right| + IR_s \quad (5.6)$$

where ΔI is a correction of the shifting of the curves from their origin along the current axis. The potential across any of these printed layers is therefore given by

$$\begin{aligned} V =& V_D(I_s) \\ &+ \left(I - \tau_s\beta - \left[\tau_s\beta - J_0 \exp\left\{ -\left(1 + \frac{R_c}{R_s}\right)^{-1} \frac{t_0}{\tau_s} \right\} \right] \exp\left\{ -\left(1 + \frac{R_c}{R_s}\right)^{-1} \frac{t}{\tau_s} \right\} \right) R_s \\ &- \Delta V, \end{aligned} \quad (5.7)$$

where ΔV is a correction of the curve shift from the origin in the voltage axis, t_0 is the hold time, J_0 is the starting time, β = current sweep/sweep delay, I_s is the reverse saturation current and $\tau_s = R_s C$. A full account and derivation of equation 5.7 has been covered by Jonah in [1]. The τ_p, R_{ps} and C values from the VI curve fitting are presented in table 5.3 below.

Table 5.3: *A comparison of (a) resistance and (b) capacitance values of mSi, SiO_2, Al_2O_3 and TiO_2 respectively*

Samples	$\tau_p(\Omega F)$		$R_{ps}(\Omega)$		C(F)	
	mn	sd	mn	sd	mn	sd
mSi	26.6	5.36	6.41E10	1.181E10	4.14E-10	1.43E-11
SiO_2	25.4	6.00	6.33E10	1.60E10	4.02E-10	1.21E-11
Al_2O_3	71.3	81.9	1.74E11	1.91E11	4.00E-10	1.39E-11
TiO_2	63.4	39.1	1.65E11	1.01E11	3.86E-10	4.91E-12

The data in table 5.3 is presented in figure 5.15, where R_g and C values are graphically compared for the respective samples.

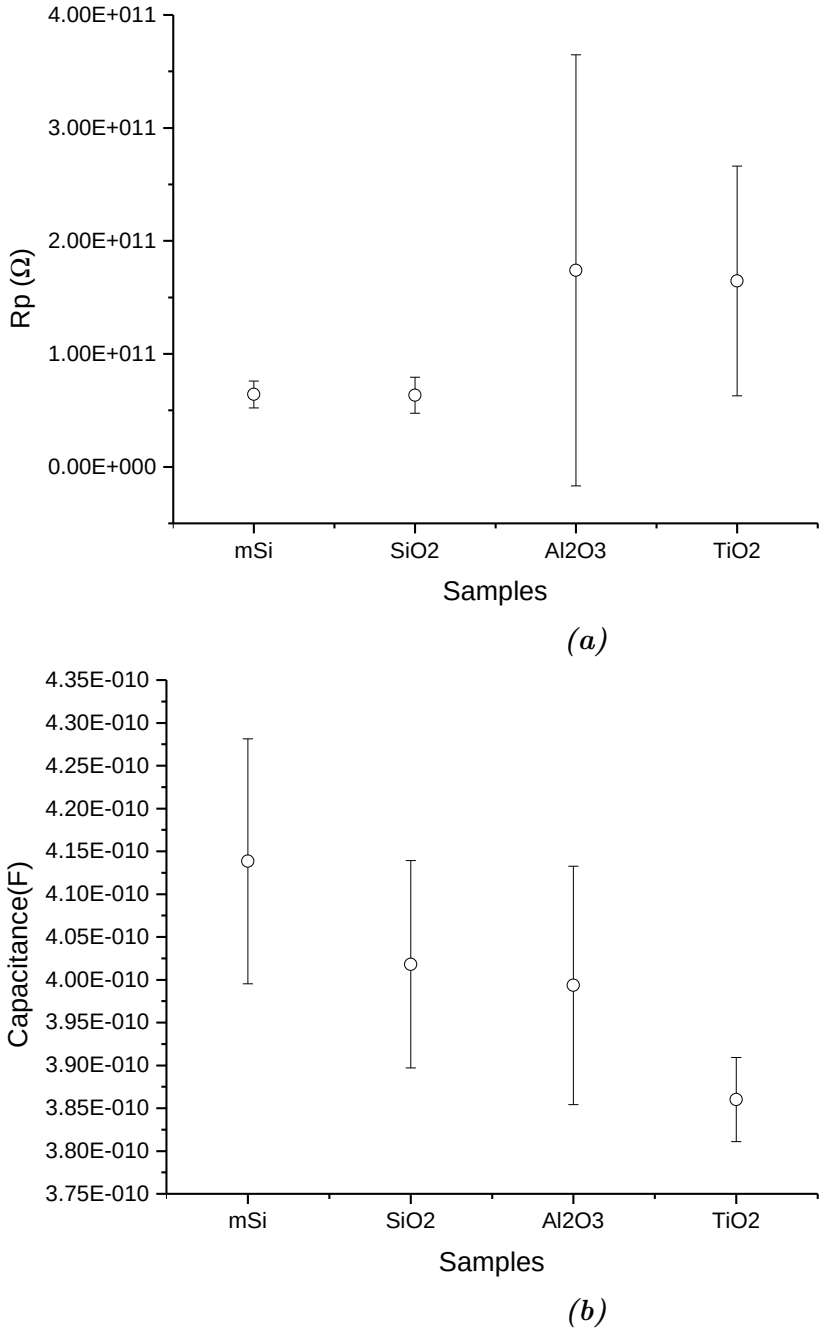

Figure 5.15: *A comparison of (a) resistance and (b) capacitance values of mSi, SiO_2, Al_2O_3 and TiO_2 respectively*

The mSi and SiO_2 samples shows comparative resistance values with generally higher capacitance values. The relative permittivity ($\epsilon_r = \epsilon_s/\epsilon_0$) is ± 11.68 for silicon and ± 3.9 for silicon dioxide. Titanium oxide has the highest $\epsilon_r \approx 86 \leftrightarrow 173$ and alumina has $\epsilon_r \approx 8.5$.

Chapter 6 Discussions

This section discusses the structural and electrical characterisation results of the materials studied. The characterisation results of the four samples will first be discussed in isolation and later compared and contrasted with one another. The main structural analysis tool, which comprised of the Unified-power law approach using equation 3.43 on p24 will be used as a pivotal point of all discussions. In this way, the fitting parameters (such as G, R_g, B, P and S/V) will be used to analyse the physical networks of nano-structured materials quantitatively. The results from other scaling models will also be used to discuss the aggregation properties of the materials [17, 42, 51]. In each case, commonalities and differences in the results from various literature and those obtained in this research will be pointed out, especially in areas where they are complementing one another.

Special focus will be placed on mSi aggregates and their influence on its electrical properties. These compact structures presented a formidable challenge in resolving individual primary particle sizes using microscopy. Nonetheless, a combination of SALS and USAXS data was used to present explicable structural properties of the materials in sizes ranging from nano to microscopic scales. In order to combine light scattering (which is based on Mie Scattering) with USAXS (which is based on Rayleigh scattering), the light scattering has been dealt with, under a severe approximation, as Rayleigh scattering.

6.1 mSi

The silicon particles were highly polydispersed, with (PDI = ± 6) and large particles of ±4 μm identifiable from the SEM micrograph in figure 6.1(a). Smaller particles generally masked bigger ones in a seemingly adhesive nature. These agglomerates followed a three-dimensional mass scaling form, which hindered SEM, being a two-dimensional imaging technique from presenting a holistic picture of the aggregate structures [41]. In addition, these mSi particles revealed larger average primary sizes than the ones previously reported by Jonah et al [1,3,32] since in this case, the particles were de-caked during the milling process. The de-caking process is suspected to have oxidized the milled mSi particles, thereby causing them to have similar resistance and capacitance values as shown in table 5.3. Although mSi particles were generally slightly smaller than SiO_2 particles and also had comparatively smaller surface to volume ratio, which led the capacitance of mSi particle to be comparable, though higher than that of SiO_2. Figure 6.1 shows the SEM and SAS results of the mSi sample.

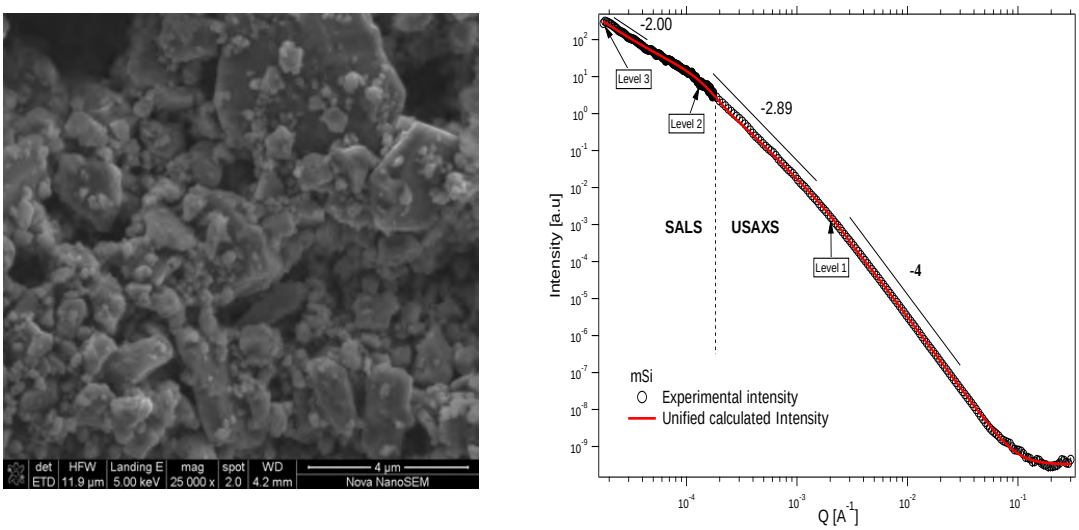

(a) SEM *(b) SAS*

Figure 6.1: *Structural characterisation of pure mSi using SALS, USAXS and SEM*

SAS results showed no noticeable difference between those obtained from printed layers and those in which powder samples were used. This became evident when the mSi SALS data obtained using a powdered glass slide extended the USAXS data seamlessly even through the USAXS data was obtained from the printed samples as shown in figure 6.1.b. As a result, two structural levels from two these exclusive events could be fitted. The first level, which represents primary particles could be used to calculate the radius

of gyration as

$$R_{g,1} \approx d_p \approx 0.1\mu m,$$

while the second level made it possible to determine the size of aggregates using

$$z = G_2/G_1 \approx 6758,$$

which is an average number of particles in an aggregate. The fractal dimension of the aggregate could be obtained from equation 2.1 on p 6 as

$$d_f = d_{min} \times c = 2.37 \times 1.12 = 2.65,$$

which implied that the particles aggregated as a mass fractal. This value agreed with the Unified power law since

$$d_f \approx P_2 = 2.85.$$

The sample also had the largest surface to volume ratio of

$$S/V \approx 57.8 \ m^2/cm^3$$

and for this reason, it displayed a higher capacitance value ($C = 0.41 \ nF$) than the other three samples as shown in figure 6.5b. The higher capacitance value of the mSi sample can be attributed to the closer gaps between the particles compared to those of SiO_2.

6.2 SiO_2

Unlike the mSi sample, SiO_2 particles had sharp edges and and there was evidence of comparatively larger particles as shown in figure 6.2a. The sharp interfaces are thought to be responsible for the relatively longer Porod region ($P = 4$) in figure 6.2b compared to that of mSi in figure 6.1b due to clear particle-to-particle interfaces. The average number of particles in SiO_2 aggregates was $z_{SiO_2} = 7681$, which was the highest of the four samples. The average size of primary particles $d_p = 0.24\mu m$, which is also comparable to the radius of gyration $R_{g,1} = 2.5\mu m$ value from the Unified fit. Therefore, the SiO_2 average primary particle sizes were more than twice that of mSi.

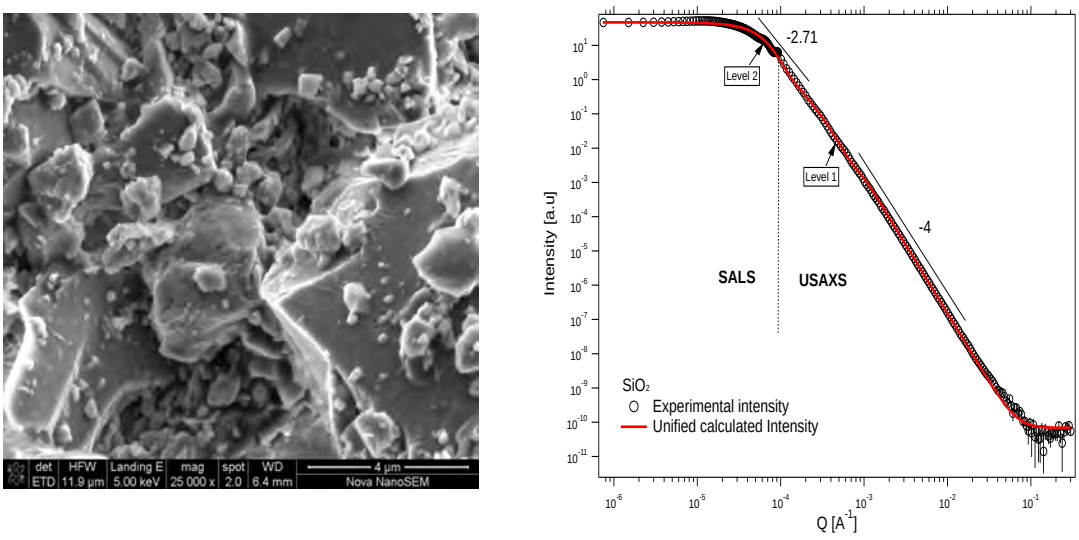

(a) SEM *(b) SAS*

Figure 6.2: *Structural characterisation of pure SiO_2 using SALS, USAXS and SEM*

The average aggregate sizes of SiO_2 particles were

$$z = G_2/G_1 \approx 7681$$

particles, with a mass fractal dimension of $d_f \approx P_2 = 2.95$ and a polydispersity index $PDI = B_1 R_{g,1}^4/1.62G_1 \approx 8.77$. The surface to volume ratio was obtained to be

$$S/V \approx 24.9 \ m^2/cm^3,$$

which it equals almost half that of mSi. This is thought to be accounting for the capacitance value of $(C = 0.40 \ nF)$ that is comparable to that of mSi particles.

6.3 Al_2O_3

The Al_2O_3 printed layers were white in colour and not stable in both PET and paper substrates. The particles were also relatively smaller compared to mSi and SiO_2 samples with a radius of gyration of $R_g \approx 140 \ nm$ as shown in figure 6.5 on p 68. The printed layer on PET resulted in higher diffuse scattering and larger background noise during the SALS experiment. After correcting for this background scattering using the scattering profile of the sample holder, the SALS data left a small gap between itself and the USAXS data as seen on figure 6.3.b after aligning the intensities of the SALS with the USAXS data. However, the Unified calculated intensity from the fit

was able to close that gap making it possible to fit three levels using the Unified power law equation.

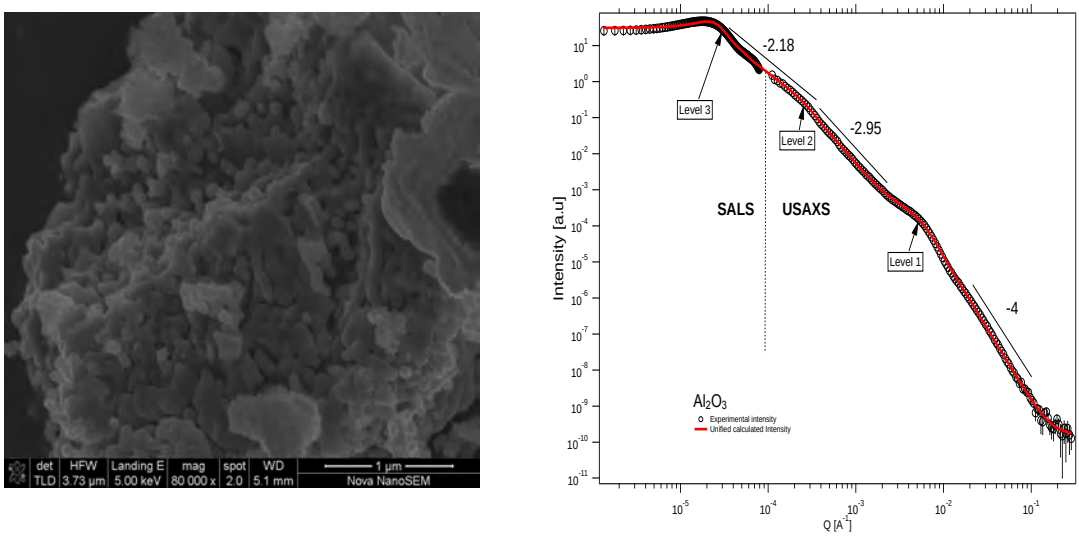

(a) *SEM* ***(b)*** *SAS*

Figure 6.3: *Structural characterisation of Al_2O_3 using (a) 80 000 × magnification SEM micrograph and (b) a combination of SALS and USAXS*

However, the Unified power-law fitting could not clearly distinguish between Al_2O_3 aggregates as particles were fused together into a smudge, thereby creating a strong dependence between particles and aggregates and their aggregates. A correlated system fitting was therefore assumed during the fitting process. The Al_2O_3 had the largest surface to volume ratio of $S/V \approx 118.38\ m^2/cm^3$. The Unified power-law did not adequately explain the morphology of the aggregates since the assumed spherical shapes in the model were far from the inherent particle shapes of this sample.

6.4 TiO_2

TiO_2 particles had relatively spherical and slightly larger primary particle sizes compared to Al_2O_3 as seen in figure 6.4. TiO_2 particles presented the least degree of polydispersity with $PDI = B_1 R_{g,1}^4 / 1.62 G_1 \approx 2.83$. The average aggregate sizes of the TiO_2 sample were obtained as

$$z = G_2/G_1 \approx 1456$$

particles with a surface fractal dimension of $d_f \approx P_2 = 3.02$. The surface to volume ratio of

$$S/V \approx 46.8 \ m^2/cm^3,$$

which although it equals almost half that of mSi, accounted for the capacitance value of $(C = 0.39 \ nF)$ that is close to that of mSi.

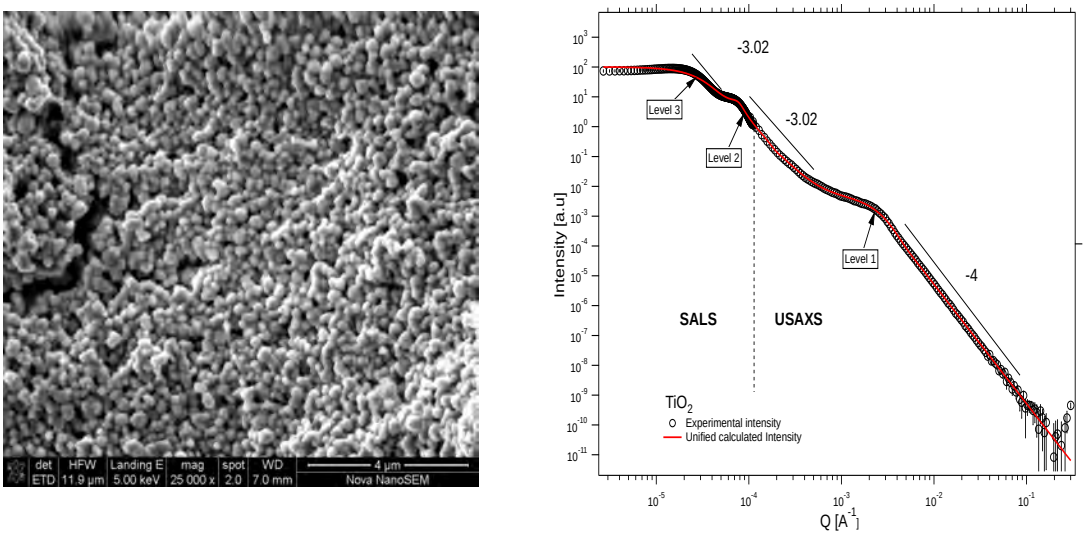

(a) *SEM* ***(b)*** *SAS*

Figure 6.4: *Structural characterisation of TiO_2 using SALS, USAXS and SEM*

Figure 6.5, shows comparative electrical properties of all four samples. The radii of gyration are compared for level one and two Unified-fitting in figure 6.5a and figure 6.5b respectively and the two level fittings are then compared against each other on figure 6.5c.

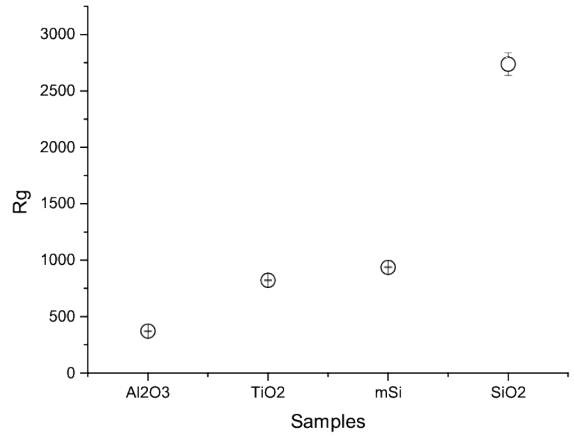

(a)

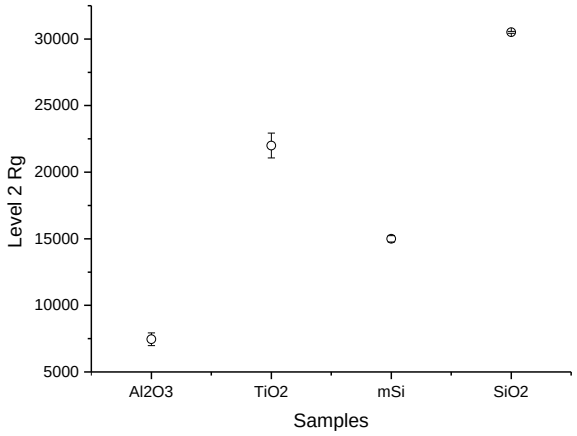

(b)

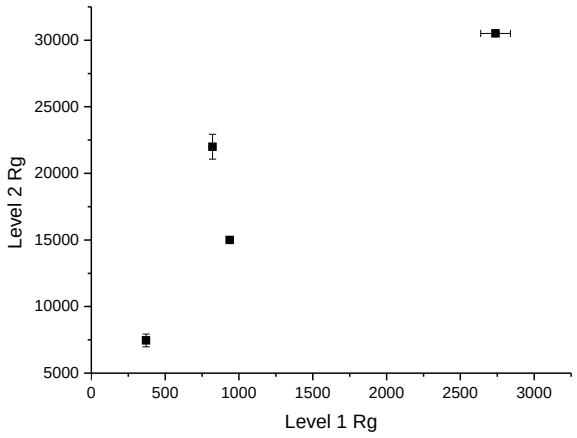

(c)

Figure 6.5: *A graphical comparison of the R_g values of pure SiO_2, Al_2O_3, mSi and TiO_2. (a) compares level 1 R_g values, (b) compares level 2 R_g values and (c) compares level 1 and level 2 R_g values against each other.*

Chapter 7 Conclusions

Particle sizes and the distribution of particle sizes in disordered materials may influence many of their properties necessary for their applications. The unified power law approach has been successfully applied to inorganic nano-structured semiconducting material (i.e mSi) and its oxide on data comprising of a combination of SALS and USAXS. At the same time, a correlation of the unified-power law SAS results with observable structural features on SEM micrographs has been successfully achieved. Each sample presented a complex arrangement of multiple related power law and Guinier regimes, representing multiple structural levels ranging from micron to nano sizes [18, 80]. The application of mass scaling laws has presented valuable quality and performance indication through mass fractal morphologies [92].

SALS, USAXS and SEM investigations were performed to characterise structural features of nano-structured materials in order to establish how they aggregated. All nano-structured materials in this research displayed varying degrees of aggregation. This aggregation of primary particles and aggregates of aggregates could not be fully exploited using any structural characterisation technique in isolation. For example, the SEM images on section 5.2 on p56 alone could not sufficiently resolve the inherent three-dimensional aggregation of the particles.

Whereas USAXS was capable of investigating the structural properties of the particles in the nano size ranges, this technique alone fell short on adequately resolving the scattering curves below $q \approx 10^{-4}$ to obtain information on aggregates as shown in figure 5.9 on p53. Furthermore, SALS alone was also capable of investigating micron particle size

ranges. However, a combination of SALS and USAXS data could extend the q-range of the SAS data by close to one order of magnitude, thereby providing the necessary leverage to exploit sizes ranging from nano to micron ranges as discussed in section 5.1.3 on p 48. The SALS data overlapped remarkably with the USAXS data thereby extending the scattering data towards the lower q-ranges, closer to the primary beam.

The Irena and Indra software packages was used to correct and de-smear the data using the lake method on the IGO pro software [89, 93]. Thereafter, the unified-fit equation 3.43 was fitted to the data.

Many researchers have in the past successfully used the SAS to characterise structural properties of complex systems of nano structures through the unified equation [18], although no evidence of SALS and USAXS combinations were found in the study of electronic semiconducting nanoparticles, particularly silicon and its oxide.

This study has demonstrated that the SAS results are independent of whether the sample was in powder form or in a printed layer form. This became evident from the SALS and USAXS data of the mSi and SiO_2 samples in figure 5.10 (a and b) on p54 which coincided with each other even though the SALS experiment was performed on powder samples while USAXS data was obtained from printed layers. Similarly, the PET and paper substrates made no difference to the results provide the scattering data of the appropriate substrate was corrected for.

Bibliography

[1] Emmanuel Ohieku Jonah. *The topology and electrical properties of nanoparticle networks*. PhD thesis, University of Cape Town, Department of Physics Faculty of Science, December 2013.

[2] U. Männl, B. Magunje, C. Van den Berg, D.T. Britton, and M. Härting, editors. *Electronic Devices Based on Printed Silicon Nanoparticles*. Proc International Conference Nanomaterials:Applications and Properties, ISSN 2304-186, 19 June 2012.

[3] D.T. Britton and M.Härting. Printed nanoparticulate composites for silicon thick-film electronics. *Pure Appl. Chem*, 78(9):1723–1739, September 2006.

[4] D.T. Britton, M. Härting, D. Knoesen, Z. Sigcau, F.P. Nemalili, T.P. Ntsoane, P. Sperr, W. Egger, and M. Nippus. Microstructural defect characterisation of a-Si:H deposited by low temperature HW-CVD on paper substrates. *Thin Solid Films*, 501(1–2):79 – 83, 2006. Proceedings of the Third International Conference on Hot-Wire {CVD} (Cat-CVD) Process Proceedings of the Third International Conference on Hot-Wire {CVD} (Cat-CVD) Process.

[5] D. K. Rai, G. Beaucage, E. O. Jonah, D. T. Britton, S. Sukumaran, S. Chopra, G. Goro Gonfa, and M. Härting. Quantitative investigations of aggregate systems. *Chem.Phys*, 137(044311):1– 4, Julu 2012.

[6] S. C. Wallwork. Scattering by a central potential. http://www.phy.ohiou.edu/~phillips/Phys735/AfnanScattering.pdf, Sep 2015.

[7] Eric D. Dahlgren. Small angle light scattering analysis of tissue. Master's thesis, Worcester Polytechnic Institute, 100 Institute Rd Worcester Polytechnic Institute Worcester, MA 01609, USA, January 2012.

[8] Ayodele Odo. *Synthesis, Characterisation and Device Application of Silicon Nanoparticles produced by Mechanical Attrition*. PhD thesis, University of Cape Town, Department of Physics, September 2009.

[9] Jan Ilavsky. Advanced photon source. http://usaxs.xray.aps.anl.gov/docs/sample_holders/.

[10] Hendrik K. Kammler, Gregory Beaucage, Roger Mueller, and Sotiris E. Pratsinis. Structure of flame-made silica nanoparticles by ultra-small-angle x-ray scattering. *Langmuir*, 20:1915–1921, October 2004.

[11] Günther Harbeke. *Polycrystalline Semiconductors: Physical Properties and Applications: Proceedings of the International School of Materials Science and Technology at the Ettore Majorana Centre, Erice, Italy, July 1–15, 1984*, volume 57. Springer Science & Business Media, 2012.

[12] F.E. Kruis, A. Goossens, and H. Fissan. Synthesis of semiconducting nanoparticles. *Journal of Aerosol Science*, 27, Supplement 1(0):S165 – S166, 1996. Abstracts of the 1996 European Aerosol Conference.

[13] PY Yu and M Cardona. Fundamentals of semiconductors: physics and materials properties. *Springer Berlin etc*, 1999.

[14] S. Baranoviski and O. Rubel. Charge transport in disordered solids with applications in electronics. In *Description of charge transport in amorphous semiconductors*, chapter 2, pages 49–93. John Wile & Sons, Ltd, Chichester, Faculty of Physics and Material Sciences Center, Philipps University Marburg, Germany, 2006.

[15] D. Stauffer and A. Aharony. Introduction to percolation theory. *Taylor and Francis London*, 1992.

[16] Scott Kickpatrick. Percolation and conduction. *Reviews of modern physics*, 45(4):574–588, March 1973.

[17] T. Freltoft, J. K. Kjems, and S. K. Sinha. Power-law correlations and finite-size effects in silica particle aggregates studied by small-angle neutron scattering. *Phys. Rev. B*, 33:269–275, Jan 1986.

[18] G. Beaucage and D.W. Schaefer. Structural studies of complex systems using small-angle scattering: a unified guinier/power-law approach. *Journal of Non-Crystalline Solids*, 172–174, Part 2(0):797 – 805, 1994. Proceedings of the Second Internatinal Discussion Meeting on Relaxations in Complex Systems.

[19] Keun Soo Kim, Yue Zhao, Houk Jang, Sang Yoon Lee, Jong Min Kim, Kwang S. Kim, Jong-Hyun Ahn, Philip Kim, Jae-Young Choi, and Byung Hee Hong. Large-scale pattern growth of graphene films for stretchable transparent electrodes. *Nature*, 457(7230):706–710, 02 2009.

[20] S.H Ko, H. Pan, C.P Grigoropoulos, C.K Luscombe, J.M.J Fréchet, and D Poulikakos. All-inkjet-printed flexible electronics fabrication on a polymer substrate by lowtemperature high-resolution selective laser sintering of metal nanoparticles. *Nanotechnology*, 18(345202), 2007.

[21] K.J Lee, B.H Jun, T.H Kim, and J Joung. Direct synthesis and inkjetting of silver nanocrystals toward printed electronics. *Nanotechnology*, 17(2427), 2006.

[22] MT Swihart. Vapor-phase synthesis of nanoparticles. current opinion in colloid & interface science. *Chemical Physics Letters*, 8:127–133, 2003.

[23] RA Bley and SM Kauzlarich. A low-temperature solution phase route for the synthesis of silicon nanoclusters. *Journal of the American Chemical Society*, 118:12461–12462, 1996.

[24] R Ghosh Chaudhuri and S Paria. Core/shell nanoparticles: classes, properties, synthesis mechanisms, characterization, and applications. *Chemical Reviews*, 112:2373–2433, 2011.

[25] R. Kelsall, I.W. Hamley, and M. Geoghegan. *Nanoscale Science and Technology*. Wiley, 2005.

[26] C. M. Keck, S. Kobierski, R. Mauludin, and R. H. Müller. Second generation of drug nanocrystals for delivery of poorly soluble drugs: Smart crystals technology. *Dosis*, 24(2):124–128, 2008.

[27] Hak-Kim Chan and Philip Chi Lip Kwok. Production methods for nanodrug particles using the bottom-up approach. *Advanced Drug Delivery Reviews*, 63(6):406 – 416, 2011. Nanodrug Particles and Nanoformulations for Drug Delivery.

[28] Suzanne M. D'Addio and Robert K. Prud'homme. Controlling drug nanoparticle formation by rapid precipitation. *Advanced Drug Delivery Reviews*, 63(6):417 – 426, 2011. Nanodrug Particles and Nanoformulations for Drug Delivery.

[29] Thomas R. Gaborski, Jessica L. Snyder, Christopher C. Striemer, David Z. Fang, Michael Hoffman, Philippe M. Fauchet, and James L. McGrath. High-performance separation of nanoparticles with ultrathin porous nanocrystalline silicon membranes. *ACS Nano*, 4(11):6973–6981, 2010. PMID: 21043434.

[30] Laura Mazzola. Commercializing nanotechnology. *Nat Biotech*, 21(10):1137–1143, 10 2003.

[31] D. T. Britton, E. A. Odo, G. Goro Gonfa, E. O. Jonah, and M. Härting. Size distribution and surface characteristics of silicon nanoparticles. *Journal of Applied Crystallography*, 42(3):448–456, Jun 2009.

[32] Magunje Batsirai. *Charge Transport in Printed Silicon Nanoparticle Networks*. Thesis, University if Cape Town, November 2012.

[33] T. Karasawa and Y. Miyata. Electrical and optical properties of indium tin oxide thin films deposited on unheated substrates by d.c. reactive sputtering. *Thin Solid Films*, 223(1):135 – 139, 1993.

[34] S. Moungthai, N. Mahadevapuram, and G. Stein. Controlling Active Layer Morphology in Polymer/Fullerene Solar Cells. In *APS Meeting Abstracts*, page 49005, February 2012.

[35] Jürgen Nelles, Dorota Sendor, Frank-Martin Petrat, and Ulrich Simon. Electrical properties of surface functionalized silicon nanoparticles. *Journal of Nanoparticle Research*, 12(4):1367–1375, 2010.

[36] Tatsuya Shimoda, Yasuo Matsuki, Masahiro Furusawa, Takashi Aoki, Ichio Yudasaka, Hideki Tanaka, Haruo Iwasawa, Daohai Wang, Masami Miyasaka, and Yasumasa Takeuchi. Solution-processed silicon films and transistors. *Nature*, 440(7085):783–786, 04 2006.

[37] Li li ZHOU, Rang su LIU, and Ze an TIAN. Simulation of formation and evolution of nano-clusters during rapid solidification of liquid ca70mg30 alloy. *Transactions of Nonferrous Metals Society of China*, 23(8):2354 – 2360, 2013.

[38] N. Sinn, M. Alishahi, and S. Hardt. Detachment of particles and particle clusters from liquid/liquid interfaces. *Journal of Colloid and Interface Science*, 458:62 – 68, 2015.

[39] Gary Nichols, Stephen Byard, Mark J. Bloxham, Joanne Botterill, Neil J. Dawson, Andrew Dennis, Valerie Diart, Nigel C. North, and John D. Sherwood. Commentarya review of the terms agglomerate and aggregate witha recommendation for nomenclature used in powderand particle characterization. *Journal of Phamaceutical Sciences*, 91(10):2103–2109, October 2002.

[40] W. Gerstner. Crystal form and particle size of organic pigments in printing inks and paints. *J. Oil Col. Chem. Assoc.*, 49:954–973, 1966.

[41] G Beaucage. Determination of branch fraction and minimum dimension of mass-fractal aggregates. *The American Physical Society*, 70(031401):1–8, September 2004.

[42] H. M. Lindsay, M. Y. LinJ, D. A. Weitz, P. Sheng, Z. Chent, R. Klein, P. Meakin, and P. Meakin. Properties of fractal colloid aggregates. *Faraday Discuss. Chem. SOC*, 83:153–165, 1987.

[43] G. Beaucage, H. K. Kammler, and S. E. Pratsinis. Particle size distributions from small-angle scattering using global scattering functions. *Journal of Applied Crystallography*, 37(4):523–535, Aug 2004.

[44] Gregory Beaucage. Toward resolution of ambiguity for the unfolded state. *Biophysical Journal*, 95(2):503–509, 2015/05/19 2008.

[45] Paul Valery. Fractals. http://www.wmip.org/fractals.html. Accessed: 2015-08-05.

[46] Benoit B. Mandelbrot. A class of multinomial multifractal measures with negative (latent) values for the "dimension" $f(\alpha)$. In pub PLENUM, editor, *Fractals physical origin and properties*, pages 3–29. Ettore Majorana Internat. Sci. Ser. Phys. Sci., 1989.

[47] Kalumbu Malekani, James A. Rice, and Jar-Shyong Lin. Comparison of techniques for determining the fractal dimensions of clay minerals. *Clays and Clay Minerals*, 44(5):677–685, 1996.

[48] Dale W. Schaefer and James E. Martin. Fractal grometry of colloids. *Physical Review Letters*, 52(26):2371–2374, june 1984.

[49] Jens C. Zahnow, Joeran Maerz, and Ulrike Feudel. Particle-based modeling of aggregation and fragmentation processes: Fractal-like aggregates. *Physica D*, 240:882–893, 5 April 2011 2011.

[50] M.J. Holler. *Power, Voting, and Voting Power*. Physica-Verlag HD, 2012.

[51] T. Freltoft, J. K. Kjems, and S. K. Sinha. Power-law correlations and finite-size effects in silica particle aggregates studied by small-angle neutron scattering. *Phys. Rev. B*, 33:269–275, Jan 1986.

[52] Jhih-Min Lin, Tsang-Lang Lin, U-Ser Jeng, Yu-Jen Zhong, Chuin-Tih Yeh, and Tsan-Yao Chen. Fractal aggregates of the Pt nanoparticles synthesized by the polyol process and poly(*N*-vinyl-2-pyrrolidone) reduction. *Journal of Applied Crystallography*, 40(s1):s540–s543, Apr 2007.

[53] Jin-Hua Zhao, Hai-Jun Zhou, and Yang-Yu Liu. Inducing effect on the percolation transition in complex networks. *Nat Commun*, 4, 09 2013.

[54] Paul J Flory. Molecular size distribution in three-dimensional polymers. vi. branched polymer containing A-R-Bf-1-type units. *Journal of the American Chemical Society*, 74(11):2718–3096, 1952.

[55] Sang Bub Lee and Jong Soo Kim. Absorbing phase transitions in diluted conserved threshold transfer process. *Phys. Rev. E*, 87:032117, Mar 2013.

[56] M.E Levishtein. The relation between critical exponents of percolation theory. *Zh. Eksp. Teor. Fiz.*, 69(05.50):396–392, July 1975.

[57] M. E. Cates. Brownian dynamics of self-similar macromolecules. *Journal de Physique*, 46(7):1059–1077, January 1985.

[58] Ying Wang, Christopher A Penfold, David A Hodgson, Miriam L Gifford, and Nigel J Burroughs. Correcting for link loss in causal network inference caused by regulator interference. *Bioinformatics*, 30(19):2779–2786, 10 2014.

[59] Qingbo Guan, Shuxing Feng, and Yanhua Ma. A network topology clustering algorithm for service identification. In *Proceedings of the 2012 International Conference on Computer Science and Service System*, CSSS '12, pages 1583–1586, Washington, DC, USA, 2012. IEEE Computer Society.

[60] P. Debye. Light scattering in solutions. *Journal of Applied Physics*, 15(4):338–342, 1944.

[61] P. Debye and A. M. Bueche. Scattering by an inhomogeneous solid. *Journal of Applied Physics*, 20(6):518–525, 1949.

[62] Guinier. A guinier. structure of age-hardened aluminium-copper alloys. *Nature*, pages 569–570, September 1938.

[63] G Porod. Die röntgenkleinwinkelstreuung von dichtgepackten kolloiden systemen. *Kolloid-Zeitschrift*, pages 83–114, 1951.

[64] G Porod. Die röntgenkleinwinkelstreuung von dichtgepackten kolloiden systemen. *Kolloid-Zeitschrift*, 2(125):108–122, February 1952.

[65] O. Kratky, E. Schaeuenstein, and A. Sekora. An unstable lattice in silk fibroin. *Nature*, 165(4191):319–320, 02 1950.

[66] O. Katky and G. Porod. Diffuse small-angle scattering of x-rays in colloid systems. *J Colloid Sci.*, 4(1):35–70, Feb 1949.

[67] H. Durchschlag, O. Kratky, O. F. Olaj, and J. W. Breitenbach. High-resolution small-angle x-ray investigations on poly-o-bromostyrene in benzene solutions. *Journal of Polymer Science: Polymer Chemistry Edition*, 11(6):1327–1338, 1973.

[68] I. Pilz, O. Kratky, A. Licht, and M. Sela. Shape and volume of anti-poly-d-alanyl antibodies in the presenc e and absence of tetra-d-alanine as followed by small-angle x-ray scattering. *Journal of Applied Crystallography*, 7(2):187–187, 1974.

[69] H.C. Hulst and H.C. van de Hulst. *Light Scattering by Small Particles*. Dover Books on Physics. Dover Publications, 1957.

[70] Kazuo Nagai. Theory of light scattering by an isotropic system composed of anisotropic units with application to the porod-kratky chain. *Polym J*, 3(1):67–83, 01 1972.

[71] The Editors of Encyclopaedia Britannica. Rayleigh-scattering. http://global.britannica.com/science/Rayleigh-scattering, July 2015.

[72] Static light scattering. http://www.lsinstruments.ch/technology/static_light_scattering_sls/, Sep 2015. Accessed: 2015-09-05.

[73] Jay Theodore Cremer Jr. 9 - coherent, elastic scatter of neutrons by atomic electric field. In Jay Theodore Cremer, editor, *Neutron and X-ray Optics*, pages 455 – 472. Elsevier, Oxford, 2013.

[74] P Storer, RS Caprari, SAC Clark, M Vos, and E Weigold. Condensed matter electron momentum spectrometer with parallel detection in energy and momentum. *Review of scientific instruments*, 65(7):2214–2226, 1994.

[75] Michel H. J. Koch, Patrice Vachette, and Dmitri I. Svergun. Small-angle scattering : a view on the properties, structures and structural changes of biological macromolecules in solution. *Quarterly Reviews of Biophysics*, 2(36):147—227, 2003.

[76] Zhang. Small-angle scattering and data analysis. http://www.soft-matter.uni-tuebingen.de/teaching/SASTutorial.pdf, note = Accessed: 2015-09-12, 2007.

[77] P Debye, H.R Anderson, and H Brumberger. Scattering by an inhomogeneous solid .ii the correlation function and its application. *Journal of applied Physics*, 28:679–683, 1957.

[78] University of Cambridge. Scattering theory. www.tcm.phy.cam.ac.uk/.../lec20-21_compress..., Scattering by a Central Potential 2015. Accessed: 2015-08-05.

[79] S. C. Wallwork. Online dictionary of crystallography. http://reference.iucr.org/dictionary/Structure_factor. Accessed: 2015-08-31.

[80] L.A. Feigin and D.I Svergun. Structure analysis by small angle x-ray scattering and neutron scattering, 1987.

[81] E. Lifshin. *X-ray Characterization of Materials*. Wiley, 2008.

[82] G. Beaucage. Approximations Leading to a Unified Exponential/Power-Law Approach to Small-Angle Scattering. *Journal of Applied Crystallography*, 28(6):717–728, Dec 1995.

[83] Schmidt P.W. Small-angle scattering studies of disordered, porous and fractal systems. *Journal of Applied Crystallography*, 2(24):414–435, 1991.

[84] Andrew J Jackson. Introduction to small-angle neutron scattering and neutron reflectometry. http://www.ncnr.nist.gov/summerschool/ss10/pdf/SANS_NR_Intro.pdf. Accessed: 2015-09-11.

[85] DY Sogah, WR Hertler, OW Webster, and GM Cohen. Group transfer polymerization-polymerization of acrylic monomers. *Macromolecules*, 20(2):1473–1488, 1987.

[86] J.S Wang, R Jérôme, P Bayard, M Patin, P Teyssie, B Vuillemin, and P Heim. Anionic polymerization of acrylic monomers. 16. living anionic copolymerization of methyl methacrylate and tert-butyl acrylate as promoted by lithium 2-(2-methoxyethoxy) ethoxide. *Macromolecules*, 27(16):4635–4638, 1994.

[87] LLC ImageMagick, Studio. ImageMagick convert command-line tool. Imaging Analysis Software, March 1999.

[88] Sean. Cambridge in colour. http://www.cambridgeincolour.com/, 2005. Accessed: 2015-10-12.

[89] Ilavsky, Jan, Jemian, and Peter R. *Irena*: tool suite for modeling and analysis of small-angle scattering. *Journal of Applied Crystallography*, 42(2):347–353, Apr 2009.

[90] Rhyme Kagiso Setshedi. Synchrotron studies (and applications) of diamond. Master's thesis, Wits University, Department of Physics, November 2011.

[91] Raymond Laagel and Olivier Haeberlé. Series and parallel combinations of diodes: Equivalence formulae and their domain of validity. http://arxiv.org/pdf/physics/0511169.pdf, 2005. Accessed: 2015-09-12.

[92] G. Beaucage. Small-Angle Scattering from Polymeric Mass Fractals of Arbitrary Mass-Fractal Dimension. *Journal of Applied Crystallography*, 29(2):134–146, Apr 1996.

[93] J Ilavsky, PR Jemian, AJ Allen, F Zhang, LE Levine, and GG Long. Ultra-small-angle x-ray scattering at the advanced photon source. *Journal of Applied Crystallography*, 42:469 –479, 2009.

Appendices

Appendix

A Image Capturing Software

```
#!/usr/bin/python
# original usb-CN07CN2C7866423J17F9A00_Laptop_Integrated_Webcam_2HDM-video-
    index0

import os
import sys

amount = input("How many pictures: ")
os.system("ls /dev/v4l/by-id")
#webcam = "usb-Apple_Inc._FaceTime_HD_Camera__Built-in__DJHCCMZ0RUDNYGB0-
    video-index0"
webcam = raw_input("Copy in webcam ID: ")
for i in range(0, amount):
        # output = "ffmpeg -f video4linux2 -i /dev/v4l/by-id/"+webcam+" -
            vframes 1 img"+‘1+i‘+".bmp"
        output = "ffmpeg -f video4mac -i /dev/v4l/by-id/"+webcam+" -vframes 1
            img"+‘1+i‘+".bmp"
        os.system(output)
os.system("mv img*.* ./Pics")
```

Appendix

B Analysis Software

```
import java.awt.*;
import java.awt.Graphics;
import java.io.BufferedWriter;

import java.io.File;
import java.io.FileNotFoundException;
import java.io.FileWriter;
import java.io.IOException;

import java.lang.IllegalStateException;
import static java.lang.String.format;

import java.util.*;
import java.util.logging.Level;
import java.util.logging.Logger;

import javax.swing.*;

public class NewClass extends JPanel {
    int             lineNum      = 0,
                    mySt         = 0,
                    xline        = 0;
    private Scanner fileIn       = new Scanner(System.in); // for reading the
```

```
    file
int             once         = 1;
int             maxIndex     = 0;
int[]           xArray       = new int[1000000];
double[]        intensArray  = new double[1000000];
ArrayList<Pixel> intensityArray = new ArrayList<Pixel>(); // array
int             countingIndex = 0;
int             yPrevious    = 0;
int             myC          = 0;
Pixel           record       = new Pixel();            // instantiating
   the pixel
Pixel           averagePixel = new Pixel();  // creating an object for
   acruing the average pixel intensities
Pixel           startPoint   = new Pixel();            // instantiating
   the starting point pixel
Pixel           endPoint     = new Pixel();            // instantiating
   the end point pixel
private Scanner input;                                 // for reading the
    file
int             ix1, ix2, iy1, iy2;                    // for the point
   that will be drawn
int             ired, igreen, iblue;                   // for the primary
    colours of the pixel
private Formatter avIntensityValues, xOutputValues;    //
private Scanner intensityInput;                        // for reading the
    maximum intensity value
String          fileInput;
double          lower_y;   // the start of vertical range for defining
   number of pixels to be averaged
double          upper_y;   // the end of vertical range for defining
   number of pixels to be averaged
double          veticalRange;                          // The number of
   pixels to be averaged vertically
double          intensity;                          // intensity of a
   pixel
double          scale; //number of pixels per cm
```

```
    String          xyString, rgbString;
    double          wavelength;                                 // the wavelength
         of light in nm
    double          sampleDistance;                            // Sample distance
         in centi meters
    String          filePath=System.getProperty("user.dir")+"/Data/";//
        declairs the file path
    String          codePath=System.getProperty("user.dir")+"/Code/";//
        declairs the file path
    private String  directoryName;
    private Formatter qValues; //output file for writting the intensity values
    Double q;
    private int i;

    // draws a point or line from the corners of the panel
   @SuppressWarnings("empty-statement")
    @Override
    public void paintComponent(Graphics g) {
        super.paintComponent(g);

////////////////////////////////////////////////////////////////////////////////////////////////////

//      open files
        if (once == 1) {

            // getting the input file
             System.out.println("1. Go to\n"+filePath);//gets the file path
            //System.out.println("1. Go to "+fileIn.next());
            System.out.println("2. Place a data file in a folder named with the
                 same name as a file");
            System.out.println("3. Place the setup file in the same foder above
                ");
            System.out.println("4. Press Any Key To Continue...");
            new java.util.Scanner(System.in).nextLine();
            System.out.println("Please enter the file name rhyme");
            String folder;
```

```
          fileInput = directoryName = fileIn.next();
         // System.out.println("\f");
          try {
              fileInput = String.format(filePath + directoryName+"/" + "%s.
                  txt", fileInput); // preparing the file input
          System.out.println(fileInput);//prints the file path

              input = new Scanner(new File(fileInput)); // file containing
                  the original picture pixels
            //  intensityInput = new Scanner(new File(codePath + "setup.txt")
                ); // file with the highest intensity pixel y value
                        System.out.println("File found");
              intensityInput = new Scanner(new File(filePath + "/" +
                  directoryName + "/" + "ExpSetup.txt")); // file with the
                  highest intensity pixel y value

          System.out.println("Now printing intensity input file path");
              System.out.println(intensityInput);//prints the intensityfile
                  path

              avIntensityValues = new Formatter(filePath + "/" +
                  directoryName + "/" + "iValues.txt"); // file containing the
                   x values acrros the constant highest intensity y value
              xOutputValues = new Formatter(filePath + "/" + directoryName +
                  "/" + "xValues.txt");
          } // end try
          catch (FileNotFoundException fileNotFoundException) {
              System.err.println("Error opening file.");
              System.exit(1);
          }                          // end catch
```

```
//
   ////////////////////////////////////////////////////////////////////////
```

```
File theDir = new File(filePath + directoryName);

  // if the directory does not exist, create it
  if (!theDir.exists()) {
    System.out.println("creating directory: " + directoryName);
    boolean result = theDir.mkdir();

     if(result) {
       System.out.println("DIR created");
     }
  }


//while(){}

//////////////////////
//          read the max inntensity value
           try {
               while (intensityInput.hasNext())
               {
                   startPoint.setXValue(intensityInput.nextInt());
                   startPoint.setYValue(intensityInput.nextInt());
                   endPoint.setXValue(intensityInput.nextInt());
                   endPoint.setYValue(intensityInput.nextInt());
                   veticalRange = intensityInput.nextDouble();
                   wavelength = intensityInput.nextDouble();
                   sampleDistance = intensityInput.nextDouble();
                   scale = intensityInput.nextDouble();
                   //scale = intensityInput.nextDouble();

               }
           } catch (NoSuchElementException elementException) {
               System.err.println("File improperly formed.");
               input.close();
```

```
            System.exit(1);
        }                           // end catch
            catch (IllegalStateException stateException) {
            System.err.println("Error reading from file.");
            System.exit(1);
        }                           // end catch

        // close the file
        if (intensityInput != null) {
            intensityInput.close(); // close file
        }

//      Establishing the upper and lower range of pixels to be averaged at
    the starting point
        lower_y = startPoint.getYValue() - veticalRange;
        upper_y = startPoint.getYValue() + veticalRange;
        System.out.println(veticalRange*2+1+" vertical pixels avaraged
            between y=" + lower_y+" and y= " + upper_y);
        //System.out.println("upper point is " + upper_y);
        yPrevious = (int) lower_y;
        intensityArray.add(record);

//      process file for displaying the maximum intensity line
        try   // read records from file using Scanner object
        {
            while (input.hasNext()) {

                // System.out.println("\n
                    !!!!!!!!!!!!!!!!!!!!!!!!!!!!!!!!!!!!\n");
                // System.out.println(input.next());
                String line = input.nextLine();

                lineNum++;
                record.setDetails(line, lineNum);
                ix1 = record.getXValue();
                ix2 = record.getXValue();
```

```
iy1 = record.getYValue();          // x1 and x2 values are
    the same so that we draw a point
iy2 = record.getYValue();          // instead of a line,
    the same as y values.



// defining the horisontal range of pixels
if ((ix1 >= endPoint.getXValue()) && (ix1 <= startPoint.
    getXValue())) {

    // beggining of vertical data collection
    if ((iy1 >= lower_y) && (iy1 <= upper_y)) {
        if ((iy1 == yPrevious + 1)) // checking end of line
            for the horizontal pixels
        {
            maxIndex     = countingIndex;
            countingIndex = 0;
            yPrevious++;
        }

        double sum = (intensArray[countingIndex] + record.
            getIntensity());

        // System.out.println(intensityArray.get(
            countingIndex).getIntensity() + " + " + record.
            getIntensity());
        // System.out.println("new value" + sum);
        // record.setIntensity(sum);
        intensArray[countingIndex] = sum;
        xArray[countingIndex]    = ix1;
        countingIndex++;
    }

    // end of the vertical data collection
}                                          // end of
    horisontal line of of pixel selection
```

```
            }                                                   // end while

            // writting to the output
            for (int p = 0; p < maxIndex; p++) {
                double answer = intensArray[p] / ((veticalRange * 2) + 1);

                avIntensityValues.format("%4.0f\n", answer); // put this
                    outside the array



            }

            for (int p = 0; p < maxIndex; p++) {

                xOutputValues.format("%4d\n", xArray[p]);  // put this
                    outside the array
            }
        }                                                       // end try
                catch (NoSuchElementException elementException) {
            System.err.println("File improperly formed.");
            input.close();
            System.exit(1);
        }                                                       // end catch
                catch (IllegalStateException stateException) {
            System.err.println("Error reading from file.");
            System.exit(1);
        }                                                       // end catch

        // end readRecords
//      ////////////////////////////////////////////////////
//      close the file
        if (input != null) {
            input.close();                                      // close input
                file
        }
```

```
if (avIntensityValues != null) {
    avIntensityValues.close();                    // close output
        file
}

if (xOutputValues != null) {
    xOutputValues.close();                        // close output
        file
}

int count = 0;
//while (count < 11) {
    try {

        //              qValues = new Formatter();
    //   File newFile = new File(filePath + "/" + directoryName +
        directoryName+".csv");//"qiValues.csv"
        File newFile = new File("/Users/rhyme/Documents/COURSES/
            PHYSICS/PHY_COURSES/PHY(UCT)/PhD Software/SALS-ANALISIS/
            Java/JavaGaipheV7/Output/" + directoryName+".csv");//"
            qiValues.csv"


        boolean createNewFile;
    createNewFile = newFile.createNewFile();
        FileWriter fileW = new FileWriter(newFile);


// int d=;

        try (BufferedWriter buffW = new BufferedWriter(fileW)) {

            for (int x = 0; x < maxIndex; x++) { // starts at zero
                and increments to max
           // for (int x = maxIndex; x >= 0; x--){ //starts at max
                and decrement to 0
```

```
                //System.out.println(q+"\n"); //To visualise the
                    qValues
                q = (4 * Math.PI / wavelength) * Math.sin(Math.atan
                    ((x / scale) / sampleDistance));
                buffW.write(q + "  ,  "); // outputting the q value
                //buffW.write(format("%f\n",q)); //This is to format
                     the output qvalues

                //outputing the intensity
                double answer = intensArray[maxIndex-x] / ((
                    veticalRange * 2) + 1);
                buffW.write(answer + "\n"); // put this outside the
                    array

            }

        } catch (IOException ex) {
        Logger.getLogger(MaxIntensity.class.getName()).log(Level.
            SEVERE, null, ex);
    }

    } catch (FileNotFoundException ex) {
        Logger.getLogger(MaxIntensity.class.getName()).log(Level.
            SEVERE, null, ex);



    } catch (IOException ex) {
    Logger.getLogger(MaxIntensity.class.getName()).log(Level.SEVERE
        , null, ex);
}



                try {
```

```
        //              qValues = new Formatter();
        File newFile = new File(filePath + "/" + directoryName +
            "/" + "qValues.txt");
        boolean createNewFile = newFile.createNewFile();
        FileWriter fileW = new FileWriter(newFile);


// int x=0;

        try (BufferedWriter buffW = new BufferedWriter(fileW)) {

            for (int x = 0; x < maxIndex; x++) {

                //System.out.println(q+"\n"); //To visualise the
                    qValues
                q = (4 * Math.PI / wavelength) * Math.sin(Math.atan
                    ((x / scale) / sampleDistance));
                buffW.write(q +"\n"); // outputting the q value
                //buffW.write(format("%f\n",q)); //This is to format
                     the output qvalues

                //outputing the intensity
              //  double answer = intensArray[x] / ((veticalRange *
                    2) + 1);
              //  buffW.write(answer + "\n"); // put this outside
                    the array

            }

        }

    } catch (FileNotFoundException ex) {
        Logger.getLogger(MaxIntensity.class.getName()).log(Level.
            SEVERE, null, ex);
```

```
            }



            catch (IOException ex) {
                Logger.getLogger(MaxIntensity.class.getName()).log(Level.
                    SEVERE, null, ex);
            }
//buffW.close();
            System.out.println( maxIndex+ " horisontal pixels analised from
                 x="+startPoint.getXValue()+" to x="+endPoint.getXValue()+"\
                nSample to screen distance = "+ sampleDistance+" mm"+"\
                nWavelength is "+wavelength+"nm\n"+"scale ="+scale+" pixels/
                cm\n\nOutput files written to \n"+filePath+"\n");




            /*   System.out.println("Sample to screen distance = "+
                sampleDistance+" mm");
            System.err.println("Sample to screen distance = "+
                sampleDistance+" mm");
            System.err.println("Output files written to \n"+filePath+"\n");
          */

           //  count++;
        //  }



          System.out.println("Done!!!!\n");
          //System.out.println("There were " + maxIndex + " lines written\n")
              ;
```

```
            once++;
            System.exit(0);

        }
    }   // end of method maximum intensity

    public static void main(String[] args) {
        MaxIntensity picture = new MaxIntensity();
        // create a new frame to hold the panel
        JFrame lineApp = new JFrame();

        lineApp.add(picture);       // add the panel to the frame
        lineApp.setSize(300, 200);  // set the size of the frame
        lineApp.setVisible(true);   // make the frame visible
        lineApp.setResizable(true); // make the frame visible
        lineApp.setDefaultCloseOperation(JFrame.EXIT_ON_CLOSE);

    }   // end main
}   // end class
```